Joule

Article

Insertion-dominated anion redox in high-capacity amorphous sulfide cathodes for solid-state batteries

Graphical abstract

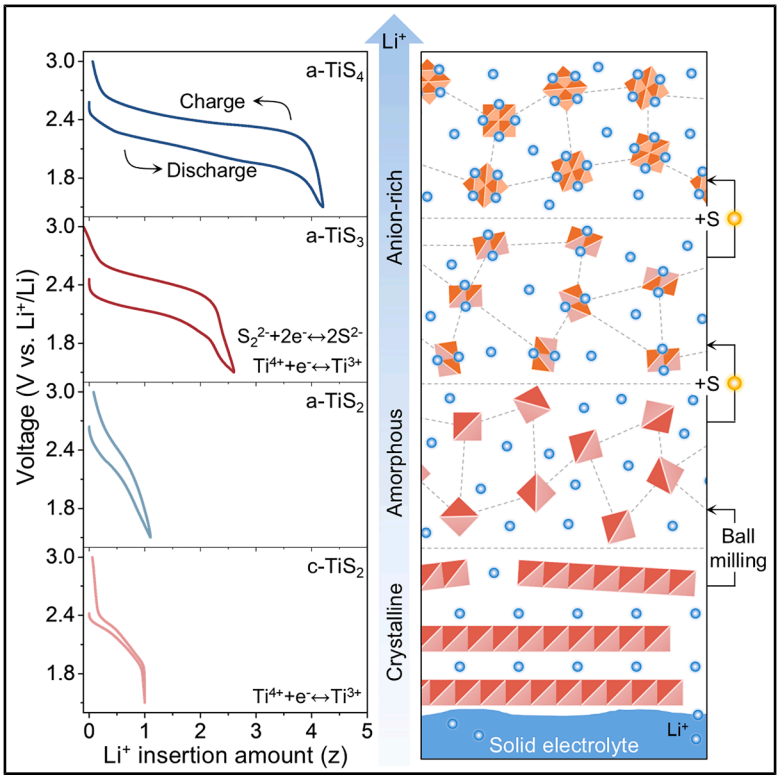

Highlights

- Integrated quasi-homogenized, amorphous, and anion-enriched cathode design
- Insertion-dominated cation-anion multi-electron redox and high interfacial stability
- High specific energy, rapid kinetics, and long-term cycling performance

Authors

Chengyu Liu, Shengan Wu, Yanjiao Ma, ..., Stefano Passerini, Yuan Ma, Yuping Wu

Correspondence

yanjiao.ma@njnu.edu.cn (Y.M.), stefano.passerini@kit.edu (S.P.), yuan.ma@seu.edu.cn (Y.M.), wuyp@seu.edu.cn (Y.W.)

In brief

Conventional cathode active materials (CAMs) often face structural and interfacial challenges when integrated into all-solid-state batteries. A sulfide-based CAM design strategy that combines interfacial compatibility, structural disorder, and anion regulation enables reversible insertion-dominated multi-electron redox chemistry, delivering high specific energy, rapid kinetics, and durable cycling performance.

Liu et al., 2027, Joule *11*, 102649
February 17, 2027
https://doi.org/10.1016/j.joule.2026.102649

CellPress

Please cite this article in press as: Liu et al., Insertion-dominated anion redox in high-capacity amorphous sulfide cathodes for solid-state batteries, Joule (2026), https://doi.org/10.1016/j.joule.2026.102649

Joule

CellPress
OPEN ACCESS

Article

Insertion-dominated anion redox in high-capacity amorphous sulfide cathodes for solid-state batteries

Chengyu Liu,[1] Shengan Wu,[2] Yanjiao Ma,[2,*] Chong Han,[3] Ke Wang,[1] Zhenqi Song,[1] Aojie Wu,[1] Chiyu Zhang,[1] Aina Zhang,[1] Stefano Passerini,[2,4,5,*] Yuan Ma,[1,6,*] and Yuping Wu[1,*]

[1]Confucius Energy Storage Lab, School of Energy and Environment & Z Energy Storage Center, Southeast University, Nanjing 211189, China
[2]International Electrochemical Energy Storage Institute (IEES), School of Energy Science and Engineering, Nanjing Normal University, Nanjing 210023, China
[3]Department of Chemistry, The University of Hong Kong, Pok Fu Lam Road, Hong Kong 999077, P.R. China
[4]Helmholtz Institute Ulm (HIU), Helmholtzstrasse 11, 89081 Ulm, Germany
[5]Karlsruhe Institute of Technology (KIT), 76021 Karlsruhe, Germany
[6]Lead contact
*Correspondence: yanjiao.ma@njnu.edu.cn (Y.M.), stefano.passerini@kit.edu (S.P.), yuan.ma@seu.edu.cn (Y.M.), wuyp@seu.edu.cn (Y.W.)
https://doi.org/10.1016/j.joule.2026.102649

CONTEXT & SCALE All-solid-state batteries (ASSBs) are promising next-generation energy storage systems because of their high safety and energy density. Their early development has been greatly accelerated by directly transferring mature cathode active materials (CAMs) from conventional batteries into solid-state configurations, particularly insertion-type chemistries such as layered oxides and Li-rich manganese-based compounds. However, these CAMs are not intrinsically designed for the distinct chemical, thermodynamic, and mechanical environment of solid electrolytes (SEs) and therefore often require surface coatings or complex multilayer SE architectures to operate effectively. Such remedies further complicate interfacial phenomena, increase processing cost, and raise barriers to practical deployment. A more fundamental solution is to design CAMs based on the intrinsic characteristics of SEs themselves. Here, focusing on sulfide SEs, we integrate interfacial quasi-homogenization, structural amorphization, and anion enrichment into a unified CAM design strategy. Using titanium (the 7th most abundant metal in the Earth's crust) sulfides as a model system, we show that matched anion chemistry homogenizes the CAMISE interface, amorphization relieves interfacial stress and accelerates ion transport, and anion regulation enables insertion-dominated cation-anion multi-electron redox. This integrated design simultaneously enhances energy density and interfacial stability, outperforming many oxide-based CAMs in terms of specific energy, rate performance, and areal capacity, and provides a general framework for the rational design of high-performance materials for practical ASSBs.

SUMMARY

Sulfide-based all-solid-state batteries (ASSBs) offer high-energy and safe energy storage, yet their performance remains limited by the structural instability of conventional crystalline cathodes and poor interfacial compatibility with sulfide solid electrolytes (SEs). Herein, we propose a synergistic cathode design integrating interfacial quasi-homogenization, structural amorphization, and anion-enrichment regulation, using titanium sulfides as a proof-of-concept system. This strategy enables insertion-dominated cation-anion multi-electron redox while promoting a chemically compatible interface and improved deformation accommodation, thereby maintaining interfacial contact during chemo-mechanical evolution and suppressing parasitic reactions. Without surface coatings or multilayer SE architectures, the selected TiS_3-based composite cathode delivers an ultrahigh capacity above 550 mAh g^{-1}, a specific energy exceeding 1,000 Wh kg^{-1}, and retains 390 mAh g^{-1} over 2,800 cycles at 2.0 A g^{-1} with ~90% capacity retention, surpassing many reported layered oxide-based cathodes. This work bridges anion chemistry, structural disorder, and interfacial stability, offering a design principle for high-performance sulfide ASSBs.

Please cite this article in press as: Liu et al., Insertion-dominated anion redox in high-capacity amorphous sulfide cathodes for solid-state batteries, Joule (2026), https://doi.org/10.1016/j.joule.2026.102649

INTRODUCTION

All-solid-state batteries (ASSBs), combining high energy density with inherent safety, have emerged as leading candidates for next-generation energy storage systems.[1–3] Among various solid electrolytes (SEs), sulfide-based SEs stand out owing to their high ionic conductivity (e.g., $\sim 1.2 \times 10^{-2}$ S cm^{-1} for $Li_{10}GeP_2S_{12}$) and excellent processability, enabling a desirable balance between power and energy output.[4–6] The selection of cathode active materials (CAMs) remains a decisive factor governing the electrochemical performance of ASSBs.[7,8] Conversion-type CAMs, such as sulfur, metal sulfides, and fluorides, can deliver high capacities through multi-electron redox reactions but often suffer from substantial volume variation and limited reversibility.[9,10] Compared with multi-electron conversion-type CAMs, single-electron crystalline insertion-type materials, such as layered oxides and halides, are widely employed because they maintain high energy density while offering moderate volume variation and stable physical contact with SEs.[11,12] Nevertheless, these materials still encounter intrinsic limitations.

First, insertion reactions are constrained by the limited storage sites and long solid-state diffusion pathways within crystalline framework.[13] Upon Li^+ insertion, the local electrostatic field becomes gradually neutralized, further slowing subsequent ion diffusion and electron transfer,[14] thereby increasing reaction barriers, polarization, and compromising overall reversibility. Second, deep Li^+ extraction often induces substantial lattice distortion and local mechanical stress evolution.[15] Such effects can trigger irreversible structural collapse or interlayer slippage, diminishing the number of active sites and accelerating degradation.[16] Accumulated stress additionally causes intergranular cracking and mechanical mismatch at the CAM|SE interface, ultimately leading to interfacial delamination and loss of electrochemical contact.[17] Third, layered crystalline CAMs exhibit pronounced chemical, thermodynamic, and mechanical mismatch with sulfide-based SEs.[18] This heterogeneity results in cation/anion diffusion and/or species loss, such as lattice oxygen release, causing the formation of resistive interphases and depletion of active species.[19] Meanwhile, the intrinsic rigidity of crystalline frameworks tends to generate electrochemically inactive interfacial regions, which progressively deteriorate during cycling and cause rapid performance decay.

Structural amorphization effectively alleviates the intrinsic limitations of ordered crystalline frameworks (Figure 1A). In amorphous structures, randomly distributed short-range ordered clusters provide abundant active sites, shorten solid-state ion diffusion pathways, and mitigate lattice distortions as well as local stress fluctuations during lithiation/delithiation.[20,21] Moreover, amorphization transforms the framework from "hard" to "soft," thereby enhancing deformation accommodation. Combined with the larger specific surface area, it enables more intimate and efficient interfacial contact with sulfide SE.[22] In parallel, to address interfacial incompatibility, an S-based quasi-homogenization (i.e., matched sulfur-based anion chemistry across the CAM|SE interface), achieved by replacing oxygen or chlorine with sulfur, reduces the chemical-potential and thermodynamic mismatch at the solid-solid heterointerface, thereby constructing a chemically more uniform CAM|SE boundary (Figure 1B, where amorphous titanium sulfides exhibit substantially suppressed interfacial reaction tendencies with $Li_{5.5}PS_{4.5}Cl_{1.5}$ (LPSC) compared with high-Ni oxide CAMs).[23,24] Although such substitution may decrease the operating voltage and energy density, enriching active sulfur anions activates anion-redox processes that compensate for this loss, accelerating local charge compensation in a multi-electron environment and improving both reaction reversibility and structural stability during cycling.[25,26]

Recognizing the strong complementarity of these optimization strategies, their synergistic integration into insertion-type CAM design holds substantial potential for enhancing ASSB overall performance (Figure 1C; Table S1). Motivated by this, the present work combines structural amorphization engineering, interfacial quasi-homogenization, and anion-enrichment strategies to construct sulfide-compatible high-performance composite cathodes. Sulfides of titanium were chosen as a model platform, enabling systematic control over both crystalline and anion richness within the TiS_x ($2 \leq x \leq 4$) series. By progressively increasing sulfur content ($TiS_2 \rightarrow TiS_4$) and introducing structural amorphization, a tunable correlation among sulfidation degree, electronic structure, and polarization behavior is established, evidencing the critical role of sulfur content in governing electron/ion transport and interfacial kinetics.

Notably, amorphous TiS_3 exhibits the most balanced electrochemical behavior with sulfide-based SE systems, delivering high capacity, excellent reversibility, and minimal polarization. *In situ* and *ex situ* characterizations further reveal reversible structural reconfiguration and an insertion-dominated multi-electron cation-anion co-storage mechanism during cycling, accompanied by adaptive interfacial stabilization at the CAM|SE boundary. This intrinsic interfacial compatibility eliminates the need for additional protective coating or complex multilayer SE architectures.[11,27] Together, the integrated framework provides a mechanistic foundation for understanding how anion chemistry, structural disorder, and interfacial energetics collectively govern electrochemical behavior in sulfide-based ASSBs and outlines a generalizable paradigm for the rational design of next-generation high-energy-density CAMs.

RESULTS AND DISCUSSION

Amorphization and anion-enrichment regulation

Amorphous and sulfur-rich titanium sulfides (a-TiS_x, x = 2, 3, 4) were synthesized via high-energy mechanochemistry by precisely controlling the ratio between crystalline TiS_2 (c-TiS_2) and sulfur (S_8) (Figure S1; detailed procedures provided in methods). Figures 2 and S2 summarize the structural amorphization features identified by scanning electron microscopy (SEM), X-ray diffraction (XRD), high-resolution transmission electron microscopy (HRTEM), and complementary analyses. As shown in the SEM image of c-TiS_2 (Figure 2A), the pristine material exhibits a block-like crystalline morphology with particle sizes exceeding 20 μm and pronounced layered structures, corresponding to long solid-state Li^+ diffusion pathways (Figure S3). After mechanochemical treatment, the particle size is markedly reduced to below 1 μm, accompanied by the original layered texture disappearance (Figures 2B and S2). The particle surfaces become noticeably smoother, and nanoscale disordered domains

Please cite this article in press as: Liu et al., Insertion-dominated anion redox in high-capacity amorphous sulfide cathodes for solid-state batteries, Joule (2026), https://doi.org/10.1016/j.joule.2026.102649

CellPress
OPEN ACCESS

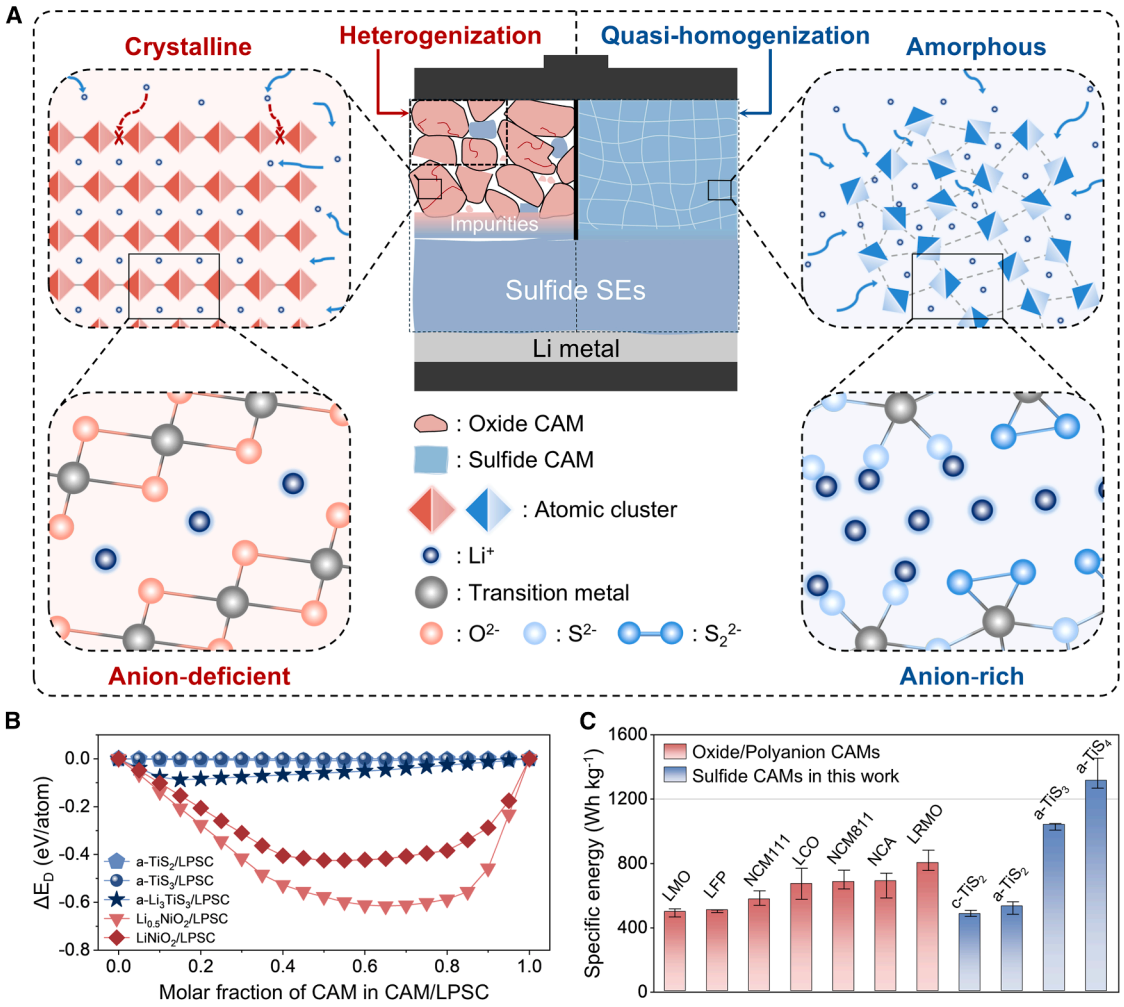

Figure 1. Quasi-homogenization-, amorphization-, and anion-enrichment-driven design for high-energy-density insertion-type sulfide CAMs

(A) Schematic comparison between crystalline oxide CAMs and amorphous insertion-type anion-rich sulfide CAMs, highlighting structural and interfacial differences.

(B) Calculated mutual decomposition energies of Li_6PS_5Cl with a-TiS_2, a-TiS_3, a-Li_3TiS_3, $Li_{0.5}NiO_2$, and $LiNiO_2$ at different mixing ratios.

(C) Comparison of specific energy (calculated based on the mass of the CAM) between mainstream oxide and polyanion CAMs and the insertion-type sulfide CAMs developed in this work for ASSBs.

emerge. This structural transformation not only shortens Li^+ diffusion pathways and substantially increases the specific surface area, increasing from 11.64 $m^2\ g^{-1}$ for c-TiS_2 to 26.53 $m^2\ g^{-1}$ for a-TiS_2 and 25.95 $m^2\ g^{-1}$ for a-TiS_3 (Figure S4), but also enhances deformation accommodation, as evidenced by the nearly 2-fold larger pressure fluctuation of c-TiS_2 relative to a-TiS_2 during cycling (discussed later in Figure 4A), thereby promoting more intimate and efficient electrochemical contact with the sulfide SEs.

XRD patterns of the synthesized products confirm their amorphous characteristics, showing the absence of distinct diffraction peaks from either the precursors or crystalline domains (Figure 2C). Although lacking long-range order, these amorphous phases retain short-range atomic coordination, providing a stable host environment for Li^+ accommodation and insertion (Figure S3).[28,29] The nanoscale structural distinctions between crystalline and amorphous phases (with a-TiS_3 taken as a representative amorphous compound) were further elucidated by HRTEM (Figures 2D and 2E). Well-defined lattice fringes with an interplanar spacing of 0.26 nm are clearly observed in c-TiS_2, whereas the amorphous counterpart displays blurred and discontinuous fringes, indicative of structural disorder. Binary image processing and statistical lattice-orientation mapping reveal that c-TiS_2 contains long (>2 nm), highly ordered fringes with an anisotropic distribution, whereas a-TiS_3 exhibits markedly shortened fringes with a broad, isotropic orientation distribution (Figures 2F and 2G).[30] Such multidirectional short-range ordering supports the formation of a more isotropic and interconnected Li^+ diffusion network, which is favorable for accelerated interfacial reaction kinetics.

Please cite this article in press as: Liu et al., Insertion-dominated anion redox in high-capacity amorphous sulfide cathodes for solid-state batteries, Joule (2026), https://doi.org/10.1016/j.joule.2026.102649

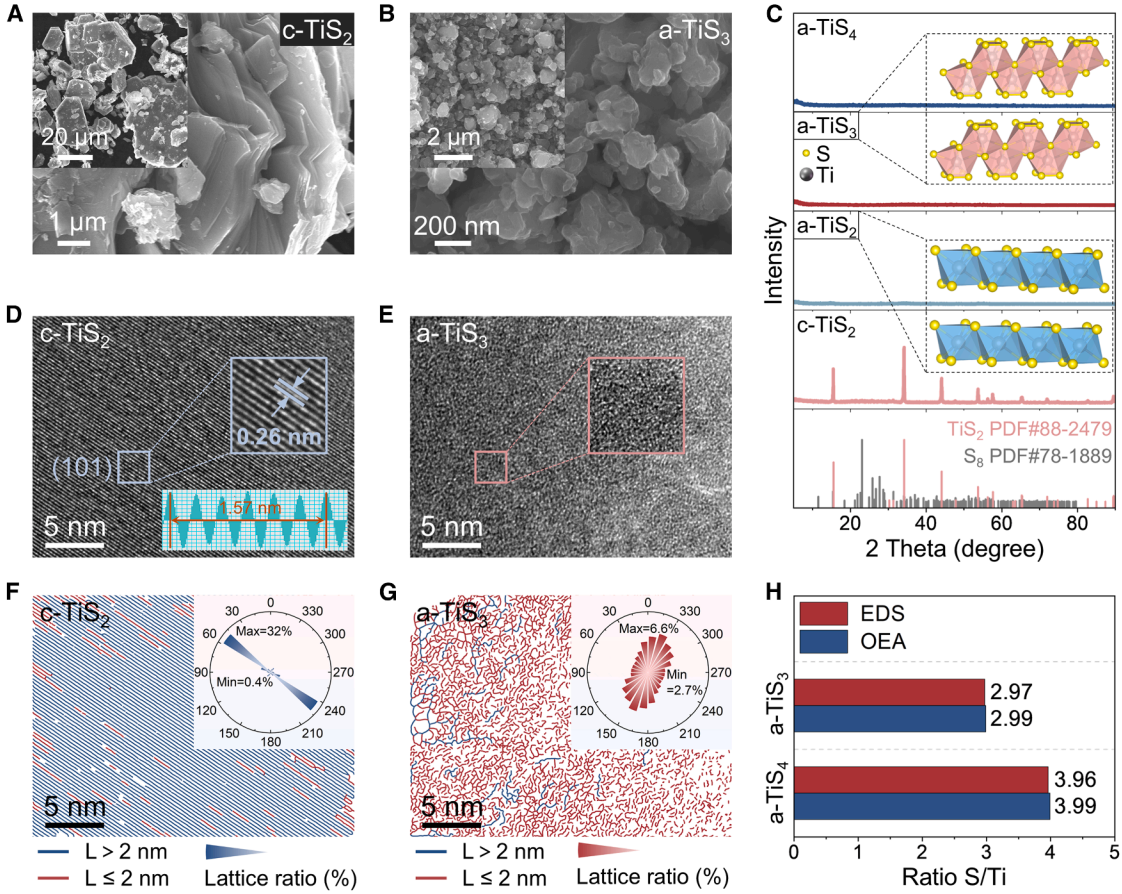

Figure 2. Structural characterization of insertion-type sulfide CAMs (titanium sulfides)

(A and B) SEM images at different magnifications of c-TiS_2 (A) and a-TiS_3 (B).

(C) XRD patterns.

(D and E) HRTEM images of c-TiS_2 (D) and a-TiS_3 (E).

(F and G) Lattice-fringe-filtered HRTEM images and corresponding lattice-orientation distributions for c-TiS_2 (F) and a-TiS_3 (G).

(H) S/Ti atomic ratios of a-TiS_3 and a-TiS_4 determined by EDS and OEA.

The compositional characteristics of titanium sulfides were further analyzed via energy-dispersive X-ray spectroscopy (EDS) and organic elemental analysis (OEA) (Figures 2H and S5; Tables S2 and S3). The measured S/Ti atomic ratios align well with the targeted stoichiometries, confirming successful synthesis of sulfur-rich compositions required for anion-enrichment. Additionally, EDS elemental mapping demonstrates homogeneous distribution of Ti and S within particles (Figure S6), indicating a complete solid-state reaction and ensuring high compositional uniformity and chemical stability.

Afterward, the compositional evolution of titanium sulfides was investigated using differential scanning calorimetry (DSC) (Figure 3A). The physical (not-milled) mixture of c-TiS_2 and S_8 exhibits sharp endothermic peaks at 119°C and 453°C, corresponding to the melting and evaporation of S_8, respectively. By contrast, both features vanish entirely in the DSC curves of amorphous products, confirming that a complete mechanochemical reaction occurred rather than forming a physical blend or inducing simple structural disorder. Raman spectroscopy provides further evidence for this transformation (Figures 3B and S7). No detectable S_8 vibrational signals remain in titanium sulfides, indicating almost full sulfur transformation during milling. Beyond compositional information, Raman analysis also elucidates changes in the bonding environment. Both crystalline and amorphous phases show the Eg mode near 150 cm^{-1}, attributed to the symmetric interlayer vibrations of titanium sulfides.[31] However, structural amorphization causes pronounced shifts in Ti–S vibrational modes: the characteristic A_1g (330 cm^{-1}) mode in c-TiS_2 disappears upon amorphization, accompanied by the emergence of broad Raman bands at higher wavenumbers (~410 and ~490 cm^{-1}).[32] These shifts reflect strengthened Ti–S interactions and a more rigid local coordination, which help stabilize the amorphous framework. Among the amorphous samples, increasing sulfur content further modifies the bonding motifs, suppressing symmetric Ti–S vibration (~490 cm^{-1}) while enhancing asymmetric ones (~410 cm^{-1}), suggesting the formation of new Ti–S coordination environments that disrupt the original lattice symmetry.

Please cite this article in press as: Liu et al., Insertion-dominated anion redox in high-capacity amorphous sulfide cathodes for solid-state batteries, Joule (2026), https://doi.org/10.1016/j.joule.2026.102649

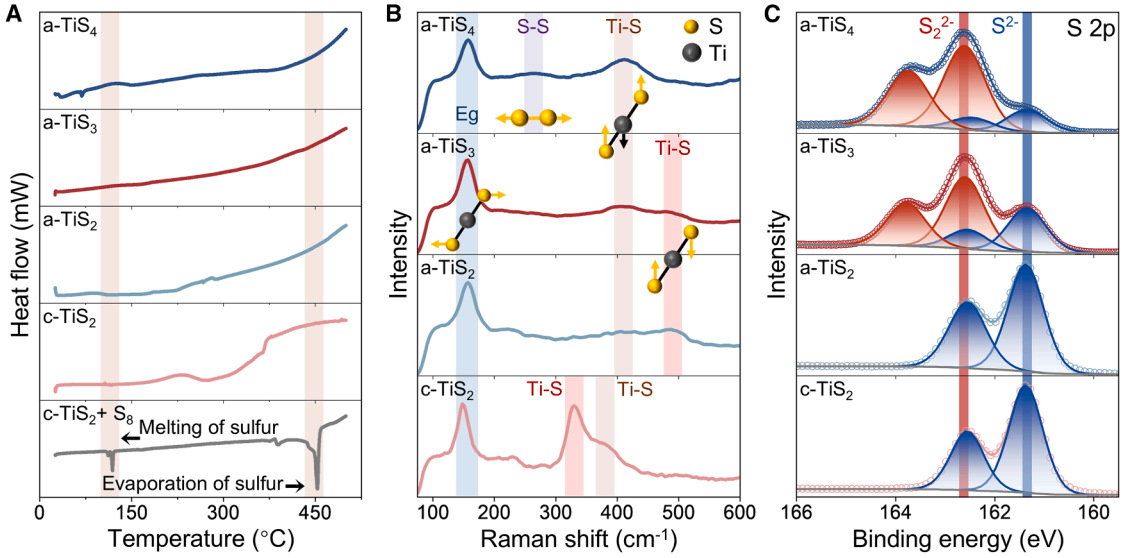

Figure 3. Physicochemical characterization of insertion-type sulfide CAMs (titanium sulfides)

(A) DSC curves.

(B) Raman spectra.

(C) S 2p XPS spectra.

Moreover, the appearance of the S–S stretching mode at ~265 cm^{-1} in a-TiS_4 signals the incorporation of polysulfide species (S_2^{2-}).[33]

Surface chemical states were analyzed by X-ray photoelectron spectroscopy (XPS) (Figure 3C). For all samples, S 2p spectra exhibit doublets at 161.4 ($2p_{3/2}$) and 162.6 eV ($2p_{1/2}$), corresponding to S^{2-} species. With increasing sulfur content, additional doublets emerge at 162.6 ($2p_{3/2}$) and 163.8 eV ($2p_{1/2}$) in a-TiS_3 and a-TiS_4, characteristic of S_2^{2-}, demonstrating the presence of sulfur in the −1 oxidation state, which corroborates the Raman results.[34] This confirms both the successful anion enrichment and the formation of titanium polysulfides within the amorphous matrix. The Ti 2p spectra display spin-orbit pairs at 455.9/462.0 and 458.5/464.6 eV, corresponding to Ti^{3+}- and Ti^{4+}-like states, respectively (Figure S8). The coexistence of these components in both crystalline and amorphous titanium sulfides reflects their complex Ti–S bonding and local electronic environments. With increasing sulfur content, the relative contribution of the Ti^{4+}-like component increases, indicating a progressively more oxidized Ti environment in the sulfur-rich amorphous samples.[35]

In addition, crystalline TiS_3 (c-TiS_3) was prepared by post-annealing ball-milled a-TiS_3 (see methods for details) to enable a comparison of the electrochemical behaviors of the crystalline and amorphous phases. As shown in Figure S9, c-TiS_3 retains a nanoscale platelet-like morphology with lateral dimensions of several hundred nanometers. The XRD pattern is readily indexed to phase-pure c-TiS_3, with no detectable impurity peaks.

Electrochemical behavior and kinetic characteristics

Building on the established structural amorphization and anion enrichment, the electrochemical behavior of titanium sulfides (c-TiS_2, c-TiS_3, and a-TiS_x [x = 2, 3, 4]) was systematically investigated. Pellet-type solid-state battery (SSB) cells were assembled using a Li-In alloy as the anode (electrochemical properties shown in Figure S10) and a high CAM loading, 4.6 ± 0.2 mg_{CAM} cm^{-2}, (corresponding to ≈1.1–3.4 mAh cm^{-2} depending on x in TiS_x). Insertion-type sulfide CAMs were uniformly incorporated into a composite matrix consisting of LPSC SE and carbon additives (detailed information is provided in methods). All cells were galvanostatically cycled at 0.05 A g^{-1} within 0.9–2.4 V vs. Li^+/InLi (i.e., ≈1.5–3.0 V vs. Li^+/Li to avoid conversion-type reactions) (Figures 4A, 4B, and S10–S12). The low current density and Li-In alloy anode configuration were selected to probe the intrinsic electrochemical response of CAMs while minimizing extrinsic effects from density, surface area variation, and anode-side interfacial instability. Lithium metal SSB cells were subsequently assembled to evaluate practical performance. The comparison of first-cycle voltage profiles clearly shows that both c-TiS_2 and a-TiS_2 undergo reversible de-/intercalation of approximately one Li^+, corresponding solely to the cationic Ti^{3+}/Ti^{4+} redox process (Figure 4A). Notably, amorphization leads to a modest capacity enhancement from 240 to 265 mAh g^{-1}, exceeding the theoretical value of 239 mAh g^{-1}, which can be attributed to the increased defect density and the greater availability of active sites. Meanwhile, the amorphous framework accommodates volume changes during cycling, thereby reducing pressure fluctuations despite the higher capacity. With higher sulfur content, additional anodic reactions are activated, enabling ~2.6 and ~4.2 Li^+ storage in a-TiS_3 and a-TiS_4, respectively, through an insertion-dominated coupled cationic-anodic (Ti^{3+}/Ti^{4+} and S^{2-}/S_2^{2-}) redox. The materials' specific capacity is substantially increased to 485 and 640 mAh g^{-1}, respectively, i.e., approaching the theoretical capacities of 558 and 761 mAh g^{-1} (corresponding to 3 and 5 Li^+ storage per formula unit). It is worth noting that, although crystalline and amorphous TiS_3 exhibit broadly similar electrochemical characteristics during the initial

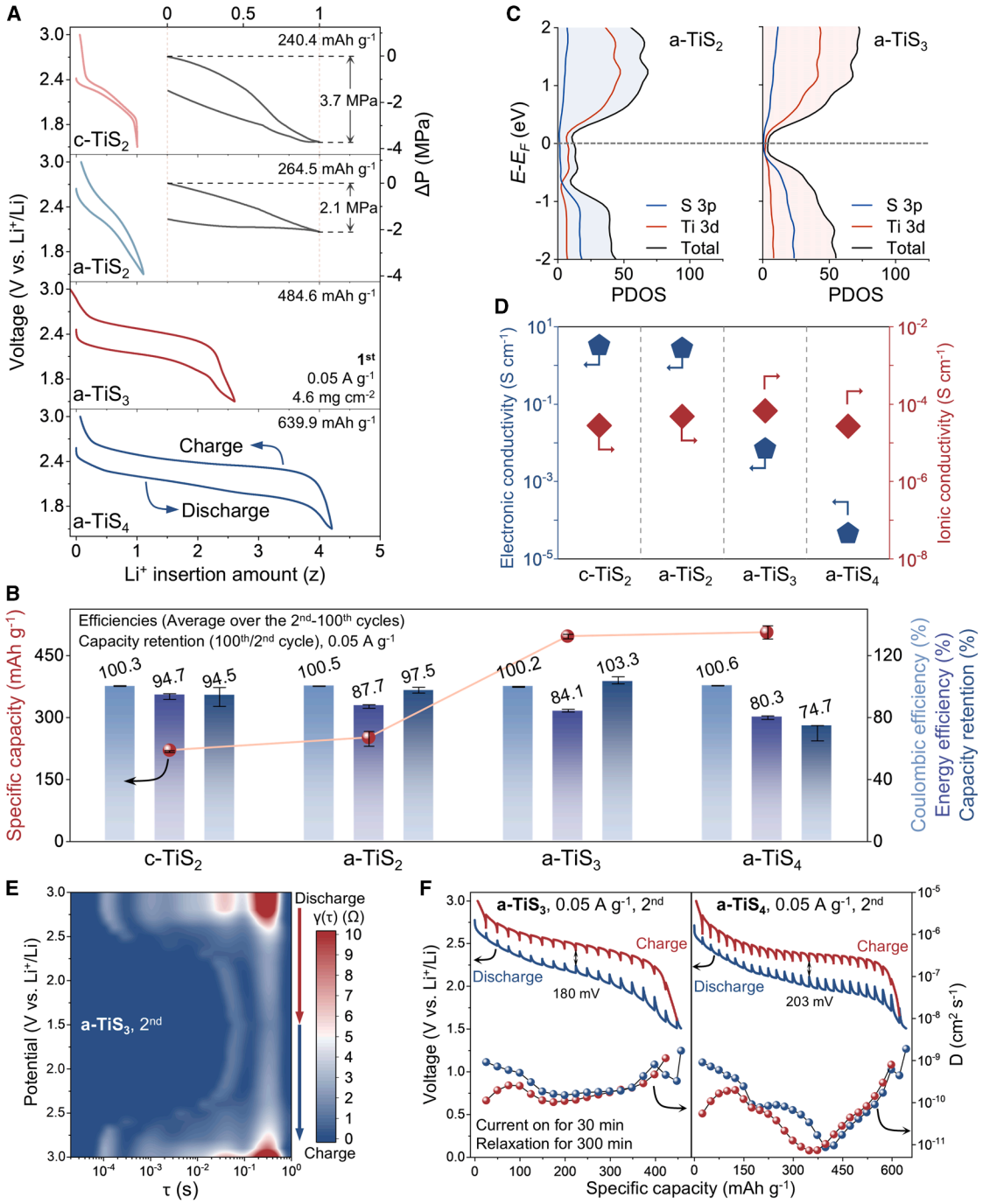

Figure 4. Electrochemical properties and reaction kinetics of titanium sulfides

(A) Initial Li^+ insertion amount and *in situ* pressure evolution at a current density of 0.05 A g^{-1}.

(B) Average specific capacity, Coulombic efficiency, and energy efficiency from 2nd to 100th cycles, along with capacity retention at the 100th cycle, at 0.05 A g^{-1}. Error bars indicate the range of values obtained from three independently tested cells for each material.

(C) PDOS of a-TiS_2 and a-TiS_3.

(D) Electronic and ionic conductivities.

(E) Contour plot of the DRT analysis of a-TiS_3 during the 2nd cycle.

(F) GITT voltage profiles and corresponding Li^+ diffusion coefficients of a-TiS_3 and a-TiS_4.

Please cite this article in press as: Liu et al., Insertion-dominated anion redox in high-capacity amorphous sulfide cathodes for solid-state batteries, Joule (2026), https://doi.org/10.1016/j.joule.2026.102649

discharge, crystallization significantly compromises both the specific capacity and reversibility (Figure S11).

Cycling performance tests over 100 cycles (Figures 4B and S12) show that c-TiS_2 delivers excellent capacity retention (94.5%) and the highest energy efficiency (>95%) among the TiS_x materials, consistent with its robust crystalline framework and high electronic conductivity (σ_e = 3.26 S cm^{-1}; Figure 4D). By contrast, amorphous TiS_x exhibit comparable or improved capacity but suffer from increased polarization and reduced energy efficiency (Figure S12), decreasing to ~88% for a-TiS_2, and further to ~84% and ~80% for a-TiS_3 and a-TiS_4, respectively. The energy efficiency loss arises from two distinct effects: amorphization-induced polarization in a-TiS_2 and progressively reduced σ_e upon sulfur enrichment in a-TiS_3 and a-TiS_4. Specifically, the transition from metallic a-TiS_2 to S–S bond-containing a-TiS_3 induces electron localization, weakens Ti 3d–S 3p hybridization, and shifts the conduction band edge upward, placing the Fermi level (E_F) within the band gap and lowering σ_e by 3–5 orders of magnitude (Figures 4C, 4D, and S13).[36,37] Despite this drawback, anion redox activation enables a-TiS_3 and a-TiS_4 to deliver high average capacities of 497 and 507 mAh g^{-1}, nearly twice those of c- and a-TiS_2. Notably, a-TiS_3 maintains ~100% capacity retention, whereas a-TiS_4 shows gradual performance fading (~0.3% per cycle), indicating reduced structural robustness at higher sulfur content. In short, amorphization coupled with sulfur enrichment markedly enhances capacity, but compromises σ_e and stability, while leaving ionic conductivity (σ_{Li^+}) largely unaffected (10^{-4}–10^{-5} S cm^{-1}) (Figures 4D and S14). Among all composites, a-TiS_3 achieves the optimal balance between capacity, stability, and efficiency.

The interface kinetics of a-TiS_x (x = 2, 3, 4) electrodes were investigated by using *in situ* electrochemical impedance spectroscopy (EIS) coupled with distribution of relaxation time (DRT) analysis (Figures 4E and S15–S19). The impedance spectra (Figures S15–S17) are dominated by a Warburg-like feature, indicating diffusion-controlled electrode kinetics.[38] The impedance decreases during lithiation and increases upon delithiation, reflecting the coupled evolution of σ_{Li^+} and σ_e. The σ_{Li^+} can be described by the Nernst-Einstein equation (Equation 1).

$$\sigma_{Li^+} = \frac{n_{Li^+} D_{Li^+} q^2}{kT} \quad \text{(Equation 1)}$$

where n_{Li^+} is the Li^+ concentration, D_{Li^+} is the Li^+ diffusion coefficient, q is the charge of Li^+, k is the Boltzmann constant, and T is the absolute temperature.

During lithiation, n_{Li^+} increases from nearly 0 to 2(x − 2) + 1 Li^+ per TiS_x formula unit, leading to a substantial enhancement in σ_{Li^+} and accounting for its initially low value in pristine a-TiS_x.

In parallel, σ_e evolution correlates with Li^+-induced coupled cation-anion redox ($Ti^{4+} \rightarrow Ti^{3+}$ and $S_2^{2-} \rightarrow 2S^{2-}$), as evidenced by the combined spectroscopic results (Figure 6). The injected electrons predominantly occupy Ti 3d states, giving rise to electronic states near E_F and narrowing the band gap, thereby enhancing σ_e, while sulfur remains electronically inactive due to its fully occupied 3p states.[39,40] Consequently, σ_{Li^+} and σ_e increase concurrently during lithiation, leading to reduced impedance, whereas the reverse trend upon delithiation reflects high reversibility.

DRT analysis was employed to investigate the state-of-charge-dependent impedance evolution (Figures 4E, S18, and S19).[41] The impedance contributions from the cathode and anode sides were distinguished using an a-TiS_3|SE|a-TiS_3 symmetric cell and a Li-In|SE|Li-In symmetric cell, revealing that the impedance response of the full cell is dominated by cathode-side processes (Figure S18).[42] With increasing lithiation depth, the overall DRT response gradually decreased, reflecting enhanced mixed ionic/electronic transport and reduced charge-transfer polarization during lithiation (Figures 4E and S19).[39,43,44] This behavior is consistent with the impedance-derived evolution of σ_{Li^+} and σ_e. Among the three materials, a-TiS_3 exhibits the lowest overall DRT intensity and the most symmetric evolution during discharge and charge, consistent with its more balanced σ_{Li^+} and σ_e (Figure 4D) and reversible structural evolution during lithiation/delithiation (Figure 6). By contrast, a-TiS_4 displays substantially larger low-frequency DRT contributions, indicating more pronounced cathode polarization.[41] Such polarization is consistent with its inferior cycling stability and rate capability observed in the subsequent electrochemical measurements (Figure 5).

Consistently, galvanostatic intermittent titration technique (GITT) measurements further confirm the superior kinetics of a-TiS_3 (Figure 4F). The sloping voltage profile with smooth potential evolution indicates a solid-solution lithiation mechanism.[45] Compared with a-TiS_4, a-TiS_3 exhibits a smaller voltage gap (~180 vs. ~203 mV), suggesting reduced polarization.[33] Quantitative analysis further shows that Li^+ diffusion coefficient of a-TiS_3 falls within the range of 10^{-8}–10^{-10} cm^2 s^{-1}, whereas that of a-TiS_4 is mainly distributed in a lower range 10^{-10}–10^{-11} cm^2 s^{-1}, demonstrating faster ionic transport and more favorable reaction kinetics for a-TiS_3.[46]

Composite cathodes' performance in ASSBs

Efficient interfacial charge transport in ASSBs fundamentally relies on intimate physical contact at the CAM|SE interface. To elucidate the intrinsic differences between crystalline and amorphous structures, titanium sulfides (c-TiS_2 and a-TiS_x [x = 2, 3, 4]) CAMs were pelletized, and their compacted density and surface porosity were systematically quantified. Owing to its larger particle size, c-TiS_2 exhibits the highest compacted density (3.26 g cm^{-3}), markedly exceeding that of amorphous counterparts (~2.5 g cm^{-3}; Figure S20), together with a minimized surface porosity, as evidenced by top-view SEM images (Figures S20 and S21). Notably, such high densification does not translate into effective interface contact: pronounced gaps are observed at the c-TiS_2|SE interface, whereas amorphous CAM (i.e., a-TiS_3) is homogeneously distributed within the SE/carbon matrix, forming a highly integrated composite structure (Figures 5A and S22). Nanoindentation measurements further show that a-TiS_2 has substantially lower hardness and Young's modulus than c-TiS_2, supporting the enhanced deformation accommodation induced by amorphization (Figure S23). Importantly, at high areal mass loading (~127 mg cm^{-2}), both composite cathodes (including a-TiS_4) show comparable thickness after densification (Figures 5B and S24), indicating that the amorphous phase accommodates deformation more effectively. This enhanced structural compliance, in synergy with the anion-enriched framework,

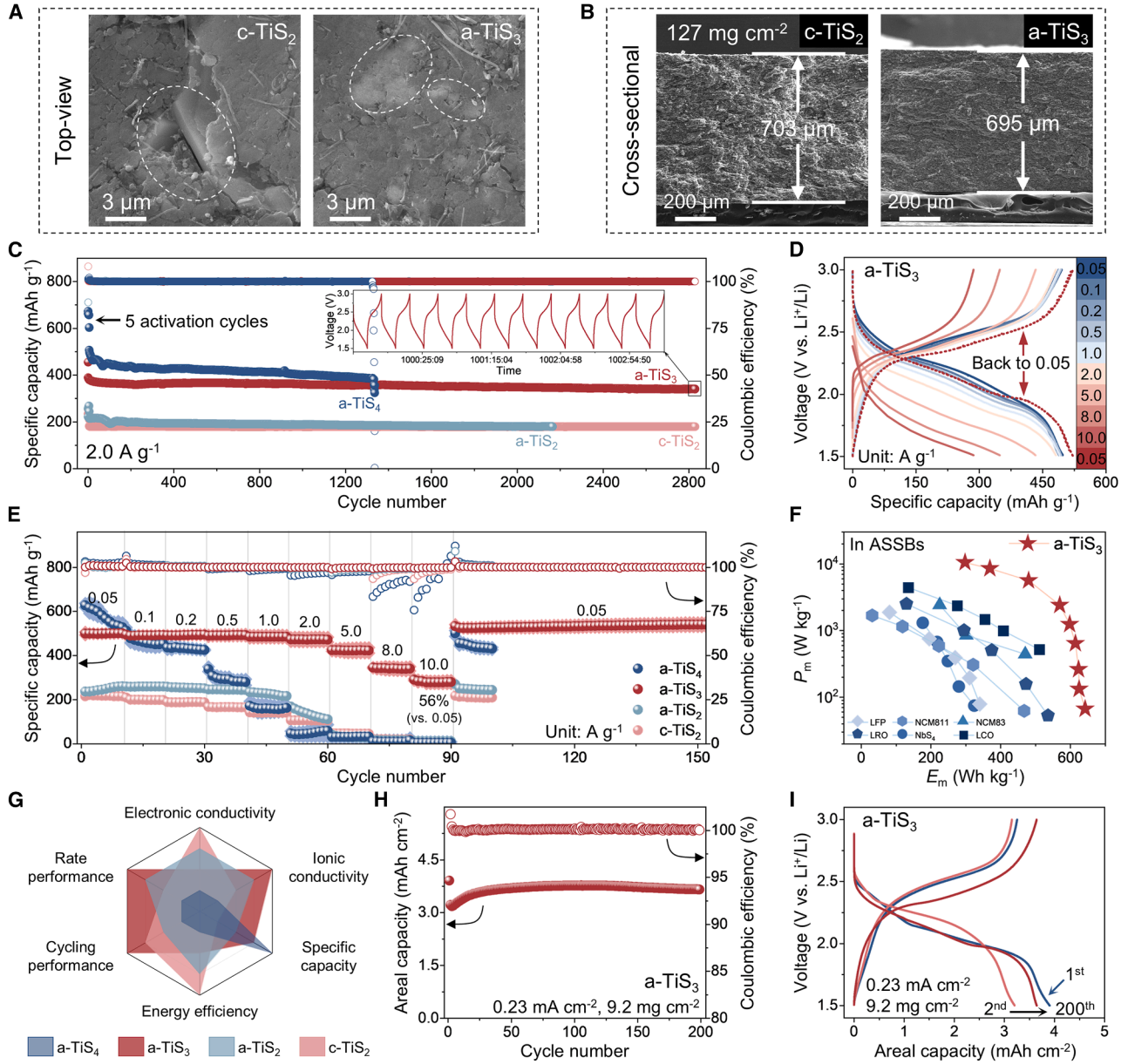

Figure 5. Comprehensive performance of titanium sulfides in ASSB composite cathodes

(A and B) Top-view (A) and cross-sectional (B) SEM images of c-TiS_2 and a-TiS_3 composite cathodes.

(C) Long-term cycling performance at a current density of 2.0 A g^{-1} after five activation cycles at 0.1 A g^{-1}.

(D) Charge-discharge profiles of a-TiS_3 at different discharge current densities.

(E) Rate performance at current densities ranging from 0.05 to 10.0 A g^{-1}. The shaded regions represent the ranges of three independently assembled cells for a-TiS_3 and a-TiS_4.

(F) Rate performance of a-TiS_3 with representative CAMs in ASSBs based on cathode-level gravimetric energy density (E_m) and power density (P_m).

(G) Radar plot comparing overall performance metrics.

(H and I) Electrochemical performance of a-TiS_3 at a CAM mass loading of 9.2 mg cm^{-2}, including discharge capacity, Coulombic efficiency (H), and charge-discharge profiles (I).

enables conformal interfacial contact and suppresses decohesion, thereby establishing a mechanically robust and electrochemically efficient and effective interface.

On the basis of the above electrochemical and physicochemical analyses, a-TiS_3 stands out with consistently superior overall performance across key metrics, which underpin its outstanding electrochemical behavior. At a current density of 0.1 A g^{-1}, a-TiS_3 delivers stable cycling over 500 cycles without obvious capacity fading, maintaining a capacity of 556 mAh g^{-1} at the 500th cycle, largely outperforming all other titanium sulfides

Please cite this article in press as: Liu et al., Insertion-dominated anion redox in high-capacity amorphous sulfide cathodes for solid-state batteries, Joule (2026), https://doi.org/10.1016/j.joule.2026.102649

(Figure S25). A similar advantage is retained at a higher current density of 2.0 A g^{-1} (Figure 5C), where a-TiS_3 sustains nearly 2,900 cycles with ~90% capacity retention, significantly exceeding the cycling performance of a-TiS_4 (~1,300 cycles). By contrast, c- and a-TiS_2 exhibit limited practical performance due to their relatively low specific capacities. The rate performance of the CAMs was evaluated by varying the discharge current density from 0.05 to 10.0 A g^{-1} (Figures 5D and 5E). At a current density of 0.05 A g^{-1}, a-TiS_3 delivers an average discharge capacity of 500 mAh g^{-1}, and notably, the capacity remains largely unchanged even when the current density is stepwise increased to 40 times its initial value. At an ultrahigh current density of 10 A g^{-1}, a-TiS_3 retains ~57% of its initial capacity, while the capacity fully recovers to ~522 mAh g^{-1} and remains stable upon reducing the current density back to 0.05 A g^{-1}, highlighting its robust structural integrity under aggressive rate conditions and outstanding rate performance. By contrast, all other titanium sulfide counterparts exhibit pronounced capacity fading at high current densities of 5–10 A g^{-1}.

To elucidate the synergistic effects of amorphization and cationic/anionic multi-electron redox, c-TiS_3 was evaluated as a structural counterpart under the same composite-cathode configuration (Figure S26). At 2.0 A g^{-1}, c-TiS_3 exhibits rapid capacity decay from ~130 to ~80 mAh g^{-1} within approximately 1,500 cycles, despite maintaining a Coulombic efficiency close to 100%. Its rate capability is also markedly inferior, with the specific capacity decreasing from ~430 mAh g^{-1} at 0.05 A g^{-1} to ~140 mAh g^{-1} at 2.0 A g^{-1} and below 60 mAh g^{-1} at 5.0 A g^{-1}. Upon returning to 0.05 A g^{-1}, the capacity recovers only partially to ~200 mAh g^{-1}. These results further demonstrate that structural amorphization markedly enhances the reaction kinetics and electrochemical reversibility of a-TiS_3.

To further benchmark this rate-capability advantage, several representative mainstream CAMs reported for ASSBs were surveyed and compared in terms of their energy density (E_m, calculated based on the composite-cathode mass) and power density (P_m) (Figure 5F; Table S4), revealing that a-TiS_3 achieves an E_m exceeding 646 Wh kg^{-1} at a P_m of 64 W kg^{-1} and remarkably maintains an E_m above 300 Wh kg^{-1} even at a high P_m of 10,420 W kg^{-1}, whereas many reported CAMs deliver only moderate E_m at low P_m followed by a rapid decline in E_m with increasing power output due to pronounced losses in reversible capacity. A comparison based on a radar chart constructed from several key indicators further demonstrates that a-TiS_3 exhibits the most balanced overall performance among four titanium sulfides CAMs, particularly in terms of reversible capacity, rate performance, and cycling stability (Figure 5G).

Finally, to evaluate its feasibility under practical operating conditions, a-TiS_3 with increased areal loading of 9.2 mg cm^{-2} delivers a high initial areal discharge capacity of ~3.9 mAh cm^{-2}. Upon cycling, the delivered capacity exhibits a gradual activation behavior followed by stable operation over 200 cycles, ultimately reaching a stable areal capacity of ~3.8 mAh cm^{-2} (Figures 5H and 5I), surpassing many previously reported ASSB cathode systems (Table S5) and further confirming the practical viability of a-TiS_3. Moreover, external pressure-free SSB cells using lithium metal as the anode were assembled to assess performance under more realistic conditions. In these cells, a-TiS_3 achieves a reversible capacity of ~450 mAh g^{-1} and an E_m approaching 580 Wh kg^{-1} (Figure S27), highlighting its promising practical applicability and robust interfacial compatibility.

Redox mechanism, structural evolution, and interfacial stability

Based on the superior overall performance of a-TiS_3, its (de)lithiation mechanism and structural evolution were systematically investigated. To elucidate the lithium-storage mechanism of a-TiS_3, a series of structural and spectroscopic characterizations were performed on a-TiS_3 electrodes at the pristine, discharged (lithiated), and charged (delithiated) states (Figures 6A–6D and S28–S30). *Ex situ* S 2p XPS spectra (Figure 6B) were employed to probe the evolution of the sulfur valence states in the a-TiS_3 electrode: in the pristine state, the dominant doublet at 162.6 eV (S $2p_{3/2}$) and 163.8 eV (S $2p_{1/2}$) is assigned to S_2^{2-}, while upon discharge to 1.5 V these peaks shift to lower binding energies of 161.4 eV and 162.5 eV, corresponding to S^{2-}, indicating sulfur reduction upon Li^+ insertion, i.e., the activation of additional anionic storage sites. Upon subsequent charging, the fraction of S^{2-} decreases, accompanied by the recovery of S_2^{2-}, evidencing reversible sulfur reoxidation.[33] S *K*-edge electron energy-loss spectroscopy (EELS) was further performed to investigate the redox evolution (Figure 6C). Compared with the pristine state, the main S *K*-edge feature shifts toward lower energy loss after discharge to 1.5 V, indicating a decrease in the average valence state of sulfur upon Li^+ insertion.[47] After subsequent charging, the feature shifts back toward its initial position, suggesting the reoxidation of sulfur. This reversible shift is consistent with the S 2p XPS results.

The evolution of the Ti oxidation state during the lithiation/delithiation process was investigated using *ex situ* Ti *K*-edge X-ray absorption near-edge structure (XANES), Ti 2p XPS, and Ti $L_{2,3}$-edge EELS (Figures 6D, S28, and S29). All three spectroscopic measurements consistently reveal the reversible evolution of the Ti oxidation state. The Ti *K*-edge XANES spectra (Figure 6D) show a pronounced absorption-edge shift of a-TiS_3 from 4,978.4 eV in the pristine state, where TiS_2 was used as a formal Ti^{4+} reference, to 4,976.9 eV after discharge, where Ti 2p XPS spectra (Figure S28) revealed the presence of Ti^{3+}.[48] This 1.5 eV shift to lower energy indicates a decrease in the average Ti oxidation state during lithiation, while comparison with the Ti metal reference excluded the complete reduction of Ti to its metallic state. Upon charging, the absorption edge largely returned toward its initial position, consistent with Ti reoxidation during delithiation. Similarly, the Ti 2p XPS spectra recover to a state closely resembling the pristine sample after charging, together with the lower-energy-loss shift of both the Ti L_3- and L_2-edge features (Figure S29) upon discharge and their return toward the pristine positions after charging, collectively confirm that Ti underwent reversible redox during the lithiation/delithiation process.[49,50] The Li 1s XPS spectra (Figure S30) exhibit a pronounced increase in intensity after discharge and a subsequent decrease upon charging, consistent with the reversible insertion/extraction of Li^+ in a-TiS_3, while the residual Li 1s signal in the pristine and charged states mainly originates from LPSC in the composite cathode.[51]

Please cite this article in press as: Liu et al., Insertion-dominated anion redox in high-capacity amorphous sulfide cathodes for solid-state batteries, Joule (2026), https://doi.org/10.1016/j.joule.2026.102649

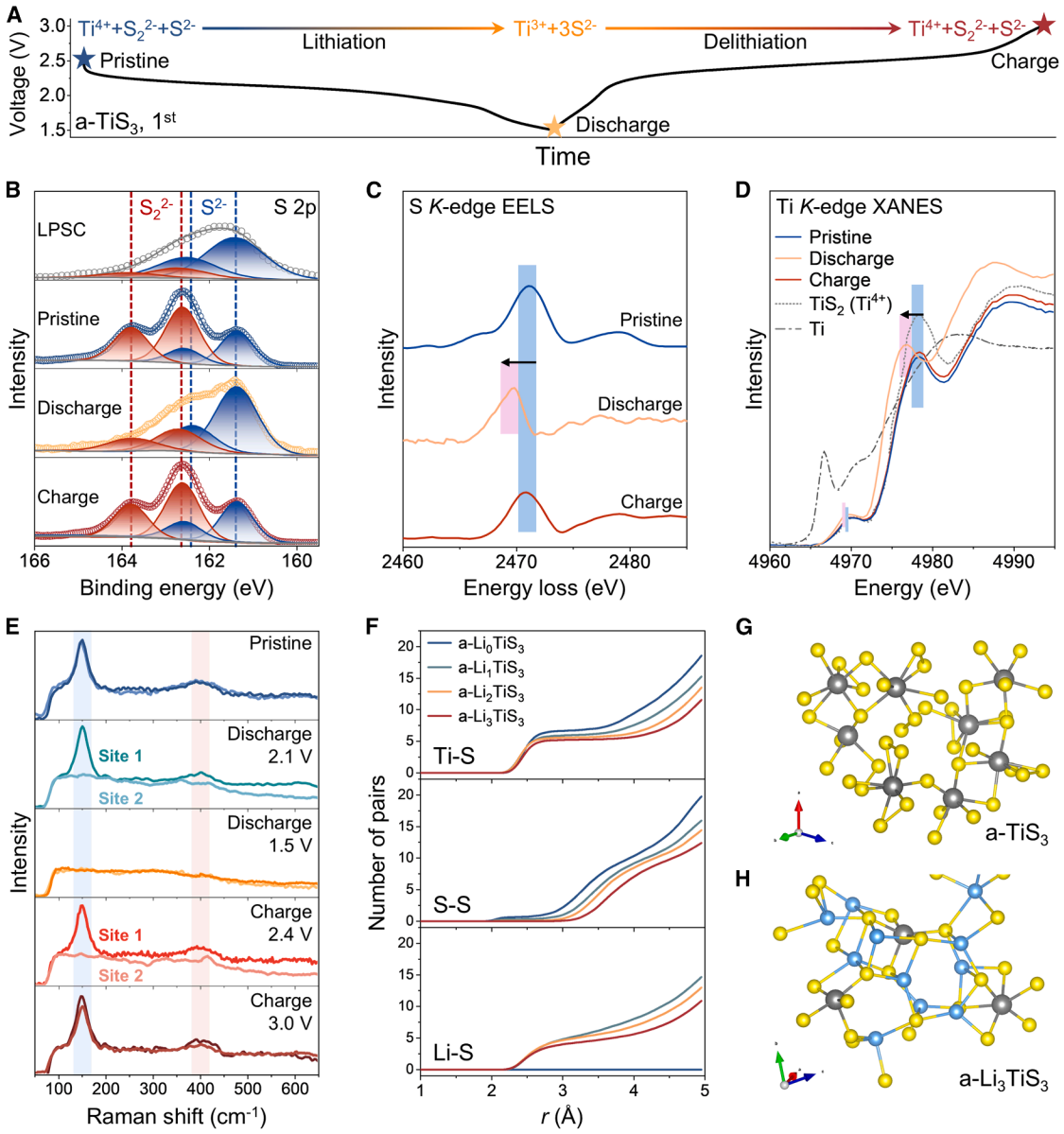

Figure 6. Lithium-storage mechanism and structural evolution of the a-TiS_3

(A) Voltage-time profiles of a-TiS_3 during the lithiation/delithiation process.

(B–D) S 2p XPS spectra (B), S *K*-edge EELS spectra (C), and Ti *K*-edge XANES spectra (D) of a-TiS_3 at the pristine, discharged, and charged states.

(E) Raman spectra at the pristine state, 2.1 and 1.5 V during discharge, and 2.4 and 3.0 V during charge, collected from two representative sites.

(F) Evolution of the Ti–S, S–S, and Li–S coordination environments in amorphous Li_xTiS_3 (x = 0, 1, 2, and 3) derived from DFT-MD simulations.

(G and H) Local structural models of (G) a-TiS_3 and (H) a-Li_3TiS_3.

Having established the reversible Ti/S redox chemistry, the structural accommodation mechanism of a-TiS_3 during Li^+ insertion/extraction process was further investigated. *Ex situ* Raman spectroscopy and density functional theory-molecular dynamics (DFT-MD) simulations were combined to investigate the structural evolution of a-TiS_3 during lithiation and delithiation, while *ex situ* XRD of c-TiS_3 was performed as a crystalline reference to provide complementary information on long-range structural changes (Figures 6E–6H, S31, and S32). *Ex situ* Raman spectroscopy (Figure 6E) shows that the pristine electrode exhibits a Raman profile nearly identical to that of the pristine powder, indicating preservation of the local structure of a-TiS_3 after composite cathode fabrication. During discharge, the broad bands at ~150 and ~400 cm^{-1} progressively weaken and become nearly undetectable at 1.5 V, suggesting pronounced lithiation-induced changes in the local vibrational environment.[52] At 2.1 and 2.4 V, spectra collected from different electrode regions show distinct responses, revealing spatially heterogeneous lithiation and

Please cite this article in press as: Liu et al., Insertion-dominated anion redox in high-capacity amorphous sulfide cathodes for solid-state batteries, Joule (2026), https://doi.org/10.1016/j.joule.2026.102649

delithiation.[53] Both bands largely recover after charging to 3.0 V, revealing a substantially reversible evolution of the local vibrational environment during lithiation and delithiation.[31,33] To complement the structural analysis of a-TiS_3, c-TiS_3 obtained by post-annealing the a-TiS_3 precursor was used as a compositionally matched crystalline reference for *ex situ* XRD analysis (Figure S31). The characteristic TiS_3 reflections remain discernible in both the discharged and charged states, without obvious diffraction peaks from new crystalline phases (e.g., Li_2S). The preservation of the characteristic TiS_3 reflections is consistent with the insertion-dominated lithium-storage mechanism proposed for a-TiS_3.

Building on these experimental observations, amorphous Li_xTiS_3 models (x = 0, 1, 2, and 3) were constructed through melt-and-quench DFT-MD simulations to examine the local structural evolution during lithiation (Figures 6F–6H and S32). With increasing Li content, the average Ti–S coordination number gradually decreases from 6.65 in a-TiS_3 to 5.21 in a-Li_3TiS_3, indicating partial rearrangement of the local Ti–S environment while substantial Ti–S connectivity is retained. By contrast, the average S–S coordination number decreases from 0.73 to 0, revealing a progressive loss of S–S coordination upon lithiation, consistent with the S_2^{2-}/S^{2-} redox process. Meanwhile, each inserted Li atom coordinates with approximately 4 to 5 S atoms, indicating the formation of extensive Li–S coordination.

Based on the above results, the Li^+ storage mechanism of a-TiS_3 is proposed as follows:

$$\text{a-}TiS_3 + xLi^+ + xe^- \leftrightarrow \text{a-}Li_xTiS_3\ (0 < x \leq 3).$$

During discharge, Li^+ inserts into a-TiS_3 to form a-Li_xTiS_3, where coupled cationic/anionic redox of Ti cations and S anions provides charge compensation through the reversible Ti^{4+}/Ti^{3+} and S_2^{2-}/S^{2-} couples.

Taken together, these complementary characterizations and simulations support an insertion-dominated lithium-storage mechanism in a-TiS_3 involving reversible local structural reconstruction. During lithiation, the initial Ti–S coordination network containing S–S linkages (Figure 6G) evolved into a locally reconstructed a-Li_3TiS_3 structure, in which S–S linkages dissociate and Li–S coordination forms, while substantial Ti–S connectivity is retained (Figure 6H).

Three-dimensional time of flight secondary ion mass spectrometry (3D TOF-SIMS) and *ex situ* P 2p XPS were employed to probe the chemical stability of the a-TiS_3|LPSC interface within the composite cathode, while *ex situ* SEM and EDS mapping were performed to evaluate the morphological integrity and elemental distribution at the composite cathode|SE interface (Figures 7A–7E, S33, and S34). The 3D TOF-SIMS reconstructions reveal spatially homogeneous distributions of PS_4^-, Li_3P^-, TiS_3^-, and LiS^- throughout both the pristine and discharged electrodes, without discernible localized accumulation of interfacial products (Figure 7A). The characteristic PS_4^- fragment is largely preserved after discharge, with a normalized discharged-to-pristine intensity ratio (I_D/I_P) of 0.95 (Figure 7B). To further evaluate possible interfacial side reactions, Li_xP^- (x = 1, 2, 3) fragments, characteristic of deeply reduced phosphorus species associated with LPSC decomposition, were analyzed.[54] Although the Li_xP^- signal shows a slight increase (I_D/I_P = 1.12), its intensity after discharge remains extremely low ($I_D < 1 \times 10^{-4}$), indicating negligible formation of reductive decomposition products and that the thiophosphate framework of LPSC remains largely intact after discharge. Similarly, the TiS_y^- (y = 2, 3) signal changes only modestly (I_D/I_P = 1.09), while the Li_zS^- (z = 1, 2) signal remains essentially unchanged (I_D/I_P = 1.01), with these minor variations providing no indication of extensive conversion involving Li_2S formation. This interpretation was further supported by the P 2p spectra, which retained the characteristic P^{5+} doublet of LPSC without additional components associated with reduced phosphorus species (Figure 7C).[55] These observations are consistent with computational results (Figure 1B), which show near-zero interfacial reaction energies between titanium sulfides and sulfide SEs compared with oxides CAM, highlighting their excellent chemical compatibility.

Ex situ SEM was employed to examine the morphological evolution of a-TiS_3-based composite cathodes before and after cycling. Top-view SEM images (Figures 7D, 7E, and S33) reveal negligible changes upon 20 cycles: LPSC appears as a dark block-like domain, a-TiS_3 remains finely and uniformly dispersed, and vapor-grown carbon fiber (VGCF) retains its rod-like morphology. High-magnification observations (Figure 7E) reveal no signs of SE decomposition or interfacial side reactions, indicating stable interfacial contact and structure during cycling. Cross-sectional SEM image and elemental mapping (Figure S34) further confirm a homogeneous Ti distribution within the composite cathode and a continuous S distribution across both composite cathode and SE separator regions, with a sharp and well-defined interface and no detectable interphase formation.

Based on these results, the lithiation process and interfacial evolution of a-TiS_3 are illustrated in Figure 7F. In the pristine state, a-TiS_3 is tightly embedded within the SE matrix, with interwoven carbon enabling continuous ionic and electronic transport. Upon lithiation, Li^+ migrates into the a-TiS_3 lattice, inducing partial S–S bond cleavage and structural disorder,[56] while the matched anionic chemistry suppresses interfacial side reactions. Further lithiation leads to Li^+ accommodation throughout the host, accompanied by partial Ti–S bond breaking and activation of Ti redox centers. Notably, the absence of a full conversion reaction limits volume change, preserves interfacial contact, maintains Li^+ transport pathways, and enables highly reversible delithiation.

Conclusions

This study proposes a comprehensive insertion-type CAM design strategy that integrates interfacial quasi-homogenization, structural amorphization, and anion-enrichment regulation to enable high-performance, long-life sulfide ASSBs. Using titanium sulfides as a representative model system, a sulfur-continuous framework is constructed to ensure strong chemical compatibility with sulfide SEs, thereby effectively mitigating interfacial degradation. The introduction of an amorphous structure further promotes compliant solid-solid contact, alleviating interfacial stress accumulation while facilitating rapid ion and electron transport. With increasing sulfur content, combined *in situ* and *ex situ* characterizations reveal a lithium-storage mechanism predominantly governed by insertion, accompanied by synergistic multi-electron redox reactions involving both cationic and anionic species. This cooperative mechanism enables

Please cite this article in press as: Liu et al., Insertion-dominated anion redox in high-capacity amorphous sulfide cathodes for solid-state batteries, Joule (2026), https://doi.org/10.1016/j.joule.2026.102649

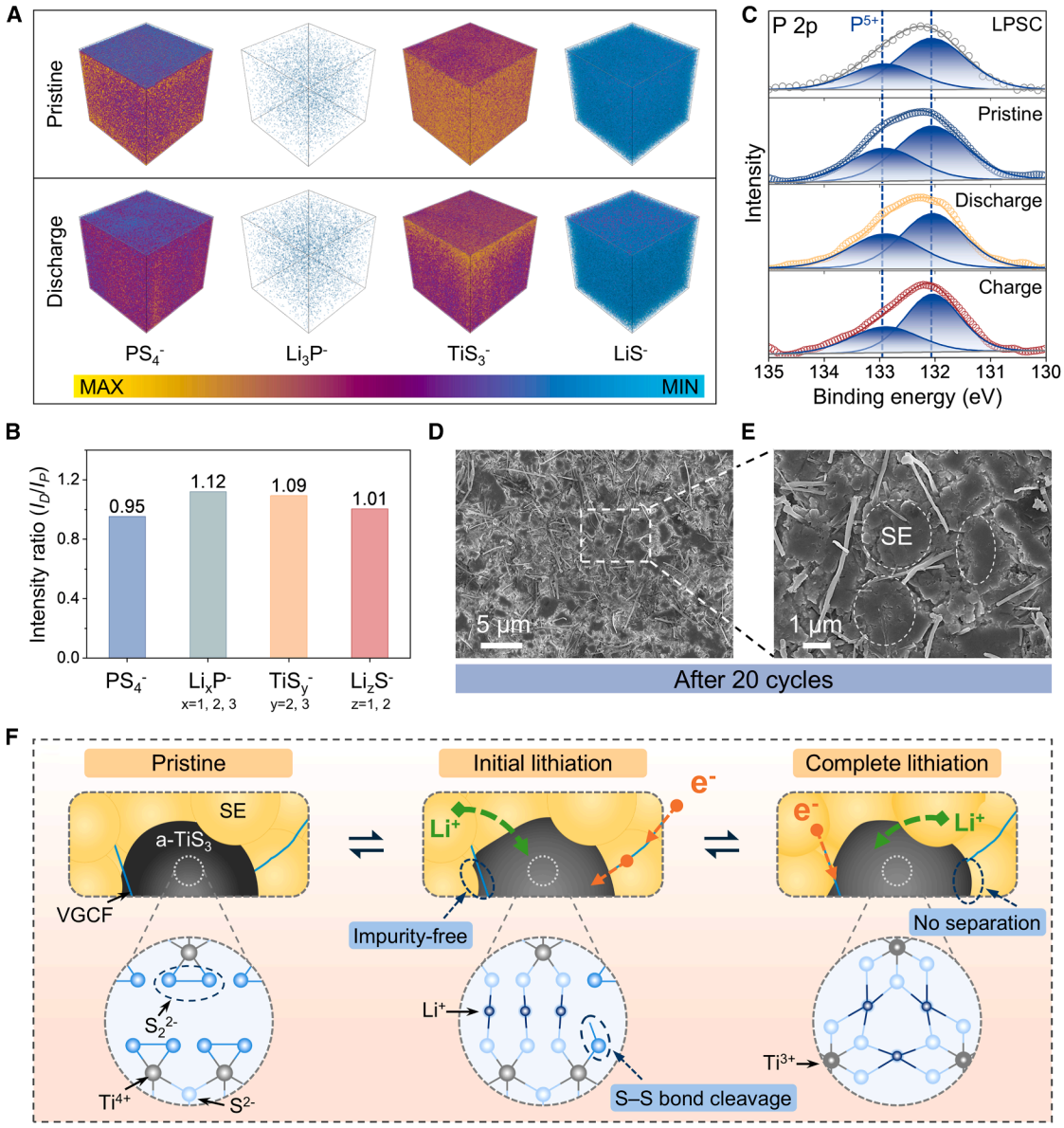

Figure 7. Interfacial stability and lithiation reaction pathway of the a-TiS_3 composite cathode

(A) 3D TOF-SIMS reconstructions of PS_4^-, Li_3P^-, TiS_3^-, and LiS^- in the pristine and discharged composite cathodes.

(B) Normalized secondary-ion intensity ratios of the discharged state relative to the pristine state (I_D/I_P).

(C) *Ex situ* P 2p XPS spectra of LPSC and the composite cathode at different electrochemical states.

(D and E) SEM images of the composite cathode after 20 cycles at different magnifications.

(F) Schematic illustration of the lithium-storage mechanism.

efficient charge compensation and enhanced redox reversibility, thereby achieving an optimal balance between high capacity and long-term stability. As a result, the selected material delivers a reversible capacity exceeding 550 mAh g^{-1}, a specific energy above 1,000 Wh kg^{-1}, and stable cycling over ~2,900 cycles at 2.0 A g^{-1}, along with promising rate capability (~300 mAh g^{-1} at 10 A g^{-1}). This work elucidates the intrinsic coupling among mechanical structure, chemical valence evolution, and interfacial stability and provides a rational design paradigm for advanced sulfide-based ASSBs.

METHODS

Materials

c-TiS_2 (99.95%, Adamas) and elemental sulfur (S_8, 99.5%, Alfa) were used as the starting materials. Amorphous titanium sulfides (a-TiS_x, x = 2, 3, and 4) were synthesized via ball milling at 510 rpm for 48 h at room temperature, using a 45 mL zirconia milling jar with a mass ratio of zirconia balls (4 mm in diameter) to raw materials of 30:1. The a-TiS_2 was directly derived from c-TiS_2 through ball milling, while a-TiS_3 and a-TiS_4 were

Please cite this article in press as: Liu et al., Insertion-dominated anion redox in high-capacity amorphous sulfide cathodes for solid-state batteries, Joule (2026), https://doi.org/10.1016/j.joule.2026.102649

prepared by co-milling c-TiS_2 with S_8 at molar ratios of 8:1 and 4:1, respectively. All material handling was conducted in an Ar-filled glovebox, and a stainless-steel air-sealed holder was employed to prevent air exposure during the milling process. c-TiS_3 was prepared by post-annealing the as-synthesized a-TiS_3. The obtained a-TiS_3 powder was sealed in an evacuated quartz tube, heated to 480°C at a ramping rate of 2°C min^{-1}, held for 6 h, and subsequently cooled to room temperature at a rate of approximately 0.76°C min^{-1}.

All-solid-state cells

Composite cathodes were prepared using c-TiS_2, c-TiS_3, and a-TiS_x (x = 2, 3, and 4) as the CAMs, with LPSC (Tianshikefeng) and VGCF (Showa) mixed at a mass ratio of 6:3:1. Taking a-TiS_3 as a representative example, 300 mg of CAMs, 150 mg of LPSC, and 50 mg of VGCF were placed in a ball-milling jar and homogenized at 150 rpm for 30 min. The cell assembly was carried out as follows: first, 80 mg of LPSC was placed into a solid-state cell mold with an inner diameter of 10 mm and pressed under 0.5 t for 2 min. The mold was then opened, and 6 mg of the composite cathode (corresponding to a mass loading of ~4.6 mg_{CAM} cm^{-2}) was added onto one side of the LPSC layer, followed by pressing under 3.0 t for 2 min. Subsequently, the opposite side of the mold was opened, and an indium foil (10 mm in diameter, 100 μm thick, Canrd) together with a lithium foil (6 mm in diameter, 200 μm thick, Canrd) was sequentially placed. The stack was then pressed until a slight movement of the pressure gauge was observed and held under this condition for 2 min. All operations were conducted in an Ar-filled glovebox. Finally, the assembled cells were placed in stainless-steel holders and subjected to a constant external pressure of 60 MPa upon electrochemical testing.

Measurements

The galvanostatic charge-discharge, rate capability, and GITT tests were conducted using a battery testing system (Neware, CT-4008Tn-5V50mA-HWX). For the rate performance tests, the first and last 10 cycles were conducted at a current density of 0.05 A g^{-1} for both charge and discharge. During the intermediate 80 cycles, galvanostatic charging was performed at 0.1 A g^{-1}, while discharging was carried out at various current densities as indicated. The voltage window was set to 0.9–2.4 V vs. Li^+/InLi (~1.5–3.0 V vs. Li^+/Li), and the measurements were performed at 30°C ± 2°C. A spoke-type load cell was positioned on one side of the SSB cell mold within the stainless-steel pressure housing. The cell was initially compressed to 60 MPa and then operated under a constant-displacement condition. After the initial pressure was applied, the pressure signal was set to zero, and the subsequent pressure variation was continuously recorded during electrochemical cycling at 0.05 A g^{-1} relative to this initial state. Electrical and ionic conductivity of the materials were measured using an electrochemical workstation (Donghua, DH7001D) at room temperature.

Characterization

The microstructures of the samples were examined by SEM (ZEISS, Sigma 360) and HRTEM (FEI, Tecnai G2 F30). Nitrogen adsorption-desorption isotherms were measured using a Physichem iPore 400 analyzer, and the specific surface areas were calculated based on the Brunauer-Emmett-Teller (BET) method. The crystal structures were characterized by powder XRD (HAOYUAN, DX-2700BH) with Cu Kα radiation. The elemental composition and ratios were determined using SEM-EDS (Bruker, Xflash Detector 730M-400) and OEA (Elementar, UNICUBE). DSC (METTLER TOLEDO, DSC 3) was conducted under an Ar atmosphere from 25°C to 500°C at a heating rate of 10°C/min. Raman spectra were collected on a WITec alpha300 R confocal Raman microscope with a 532 nm excitation laser. The surface chemical states were analyzed by XPS (Thermo Fisher Scientific, ESCALAB Xi^+), and the binding energies were calibrated against the C 1s peak at 284.8 eV. Scanning transmission electron microscopy-electron energy-loss spectroscopy (STEM-EELS) analysis was performed on a Spectra 300 (S)TEM system (Thermo Fisher Scientific). XANES spectra were collected using a Rapid-XAFS 1M system (Anhui Absorption Spectroscopy Analysis Instrument). TOF-SIMS measurements were performed on an IONTOF M6 instrument (IONTOF) using Bi_3^+ primary ions with an ion energy of 30 keV and an ion current of 0.30 pA. The analysis area was 50 × 50 $μm^2$, and the mass range was collected from 0 to 1,000 u in spectrometry mode. For depth-profiling measurements, the sputtering crater area was set to 250 × 250 $μm^2$. All samples were transferred under Ar protection and tested under either a vacuum or Ar atmosphere to avoid exposure to air.

Calculations

All *ab initio* molecular dynamics (AIMD) simulations and DFT calculations for the amorphous titanium sulfide models were performed using the Vienna Ab initio Simulation Package (VASP) within the projector augmented-wave (PAW) framework.[57–60] The exchange-correlation interaction was described using the Perdew-Burke-Ernzerhof generalized gradient approximation (GGA-PBE), together with the DFT-D3 dispersion correction to account for van der Waals interactions.[61,62] A Hubbard correction of (U_{eff} = 3.0) eV was applied to the Ti 3d states. The plane-wave energy cutoff was set to 450 eV. Owing to the large amorphous supercells, Brillouin-zone sampling was restricted to the Γ point.

Amorphous TiS_2 and Li_xTiS_3 (x = 0, 1, 2, and 3, where x = 0 corresponds to TiS_3) models were generated using a melt-and-quench AIMD procedure. The initial structures were heated to 3,000 K and equilibrated for 20 ps in the canonical (NVT) ensemble using a Nosé-Hoover thermostat and a time step of 1 fs.[63,64] The resulting configurations were then rapidly quenched to 300 K and further equilibrated for 10 ps. After AIMD, the final structures were fully relaxed before subsequent electronic-structure and local-coordination analyses.

Phase-diagram construction and interfacial reaction-energy analysis were performed using the pymatgen package.[65] The locally calculated energies of a-TiS_2, a-TiS_3, and Li_3TiS_3 were aligned with the Materials Project GGA+U energy scheme to ensure consistency with the database-derived competing phases. To account for the intrinsic metastability of the amorphous structures, an energy penalty of 0.05 eV $atom^{-1}$ relative to the corresponding crystalline convex-hull energies was applied to all amorphous titanium sulfide phases. Crystalline

$Li_{0.5}NiO_2$ and $LiNiO_2$, together with Li_6PS_5Cl and the relevant decomposition products, were described using the corresponding Materials Project entries.

The thermodynamic compatibility between Li_6PS_5Cl and electrode materials (a-TiS_2, a-TiS_3, a-Li_3TiS_3, $Li_{0.5}NiO_2$, and $LiNiO_2$) was evaluated using the mutual reaction energy scheme proposed by Mo et al.[66] The interface was modeled as a pseudo-binary system with a normalized composition $C_{interface}$ determined by the molar fraction x of the SE:

$$C_{interface} = x \cdot C_{SE} + (1 - x)C_{electrode}.$$

The total decomposition energy of the interface, $\Delta E_D(SE, electrode, x)$ was calculated by comparing the energy of the thermodynamic phase equilibria on the compositional convex hull E_{eq} with the linear combination of the original component energies:

$$\Delta E_D(SE, electrode, x) = E_{eq}\,(C_{interface}) - [x\,E(SE) + (1 - x)E(electrode)].$$

To explicitly evaluate the chemical compatibility between the two materials, the mutual reaction energy $\Delta E_{D,mutual}$ was determined by subtracting the inherent decomposition energies of the individual SE and electrode phases $\Delta E_D(SE)$ and $\Delta E_D(electrode)$ from the total decomposition energy:

$$\Delta E_{D,mutual}(SE, electrode, x) = \Delta E_D(SE, electrode, x) - x\Delta E_D(SE) - (1 - x)\Delta E_D(electrode).$$

The molar fraction x was varied from 0 to 1 to simulate different interfacial contact conditions. The minimum value of the mutual reaction energy across all mixing ratios was identified to evaluate the maximum thermodynamic driving force for interfacial decompositions:

$$\Delta E_{D,min,mutual} = \min_{x \in (0,1)} \left[\Delta E_{D,mutual}(SE, electrode, x)\right].$$

Highly negative $\Delta E_{D,min,mutual}$ values indicate a strong thermodynamic driving force for the formation of decomposition interphase layers, whereas values close to zero suggest good intrinsic chemical compatibility.

The relaxed amorphous TiS_2 and TiS_3 structures were used for projected density of states (PDOS) calculations to evaluate their electronic structures. The PDOS was projected onto the Ti 3d and S 3p orbitals, and the Fermi level was aligned to 0 eV. For the amorphous Li_xTiS_3 models, the local structural evolution during lithiation was analyzed by calculating the Ti–S, S–S, and Li–S radial distribution functions and corresponding coordination numbers. The cutoff radii for Ti–S, S–S, and Li–S coordination analyses were determined from the first minima after the corresponding peaks in the partial radial distribution functions and set to 3.0, 2.5, and 3.0 Å, respectively, ensuring that only the first coordination shell was included.

RESOURCE AVAILABILITY

Lead contact

Requests for further information and resources should be directed to, and will be fulfilled by, the lead contact, Yuan Ma (yuan.ma@seu.edu.cn).

Materials availability

- This study did not generate any new, unique materials.
- Materials generated in this study are available from the lead contact upon reasonable request.

Data and code availability

- All data needed to evaluate the conclusions in the paper are present in the paper and/or the supplemental information.
- The electrochemical datasets generated in this study are publicly available in the Zenodo repository (Zenodo: https://doi.org/10.5281/zenodo.21766760).
- This paper does not report original code.
- Any additional information required to reanalyze the data reported in this paper is available from the lead contact upon request.

ACKNOWLEDGMENTS

The research was supported by the National Key R&D Program of China (2021YFB2400400), the National Natural Science Foundation Committee of China (key project of 52131306), the Project on Carbon Emission Peak and Neutrality of Jiangsu Province (BE2022031-4), the Research Start-up Fund of Nanjing Normal University (184080H201B41), and the Research Start-up Fund of Southeast University (RF1028624081). S.P. acknowledges the Helmholtz Association's basic funding. The authors thank the Hong Kong Quantum AI Lab and AIR@InnoHK of the Hong Kong Government for providing computational resources. The authors thank Nanjing Lu-Nan Navi Technology Co., Ltd. (https://www.navi-sci.cn/) for assistance with XPS, STEM-EELS, XANES, and TOF-SIMS.

AUTHOR CONTRIBUTIONS

C.L. and Yuan Ma conceived the project. C.L. and Yuan Ma designed the research, synthesized the materials, carried out electrochemical measurements, and performed part of the physical characterizations. C.L. analyzed the data and wrote the original draft. S.W. and C.H. performed the theoretical calculations. K.W., Z.S., A.W., C.Z., and A.Z. assisted with physical characterizations. S.P., Yuan Ma, and Y.W. contributed to the discussion and interpretation of the results and revised the manuscript. Yuan Ma and Y.W. provided financial support and research resources. Yanjiao Ma, S.P., Yuan Ma, and Y.W. supervised the project. All authors discussed the results and approved the final manuscript.

DECLARATION OF INTERESTS

The authors declare no competing interests.

SUPPLEMENTAL INFORMATION

Supplemental information can be found online at https://doi.org/10.1016/j.joule.2026.102649.

Received: April 24, 2026
Revised: July 13, 2026
Accepted: August 6, 2026

REFERENCES

1. Manthiram, A., Yu, X., and Wang, S. (2017). Lithium battery chemistries enabled by solid-state electrolytes. Nat. Rev. Mater. *2*, 1–16. https://doi.org/10.1038/natrevmats.2016.103.
2. Song, Z., Ma, Y., Cheng, X., Zhu, Z., Zhong, Y., He, J., Wang, T., Xu, D., Zhang, Q., Ozoemena, K.I., et al. (2025). Development of advanced anodes for solid-state lithium batteries. Mater. Today *88*, 1005–1027. https://doi.org/10.1016/j.mattod.2025.06.041.

3. Sun, C., Liu, J., Gong, Y., Wilkinson, D.P., and Zhang, J. (2017). Recent advances in all-solid-state rechargeable lithium batteries. Nano Energy *33*, 363–386. https://doi.org/10.1016/j.nanoen.2017.01.028.

4. Zhang, Q., Cao, D., Ma, Y., Natan, A., Aurora, P., and Zhu, H. (2019). Sulfide-Based Solid-State Electrolytes: Synthesis, Stability, and Potential for All-Solid-State Batteries. Adv. Mater. *31*, e1901131. https://doi.org/10.1002/adma.201901131.

5. Chen, S., Xie, D., Liu, G., Mwizerwa, J.P., Zhang, Q., Zhao, Y., Xu, X., and Yao, X. (2018). Sulfide solid electrolytes for all-solid-state lithium batteries: Structure, conductivity, stability and application. Energy Storage Mater. *14*, 58–74. https://doi.org/10.1016/j.ensm.2018.02.020.

6. Kato, Y., Hori, S., Saito, T., Suzuki, K., Hirayama, M., Mitsui, A., Yonemura, M., Iba, H., and Kanno, R. (2016). High-power all-solid-state batteries using sulfide superionic conductors. Nat. Energy *1*, 1–7. https://doi.org/10.1038/nenergy.2016.30.

7. Chen, X., Li, X., Luo, L., He, S., Chen, J., Liu, Y., Pan, H., Song, Y., and Hu, R. (2023). Practical Application of All-Solid-State Lithium Batteries Based on High-Voltage Cathodes: Challenges and Progress. Adv. Energy Mater. *13*, 2301230. https://doi.org/10.1002/aenm.202301230.

8. Wang, S., Liu, S., Chen, W., Hu, Y., Chen, D., He, M., Zhou, M., Lei, T., Zhang, Y., and Xiong, J. (2024). Designing Reliable Cathode System for High-Performance Inorganic Solid-State Pouch Cells. Adv. Sci. (Weinh) *11*, e2401889. https://doi.org/10.1002/advs.202401889.

9. Wang, L., Wu, Z., Zou, J., Gao, P., Niu, X., Li, H., and Chen, L. (2019). Li-free cathode materials for high energy density lithium batteries. Joule *3*, 2086–2102. https://doi.org/10.1016/j.joule.2019.07.011.

10. Li, Z., Zhou, G., Li, S., Liu, H., Wang, L., and Li, H. (2023). Unlocking cycling longevity in micro-sized conversion-type FeS_2 cathodes. Joule *7*, 2609–2621. https://doi.org/10.1016/j.joule.2023.10.003.

11. Ma, Y., Zhang, R., Tang, Y., Ma, Y., Teo, J.H., Diemant, T., Goonetilleke, D., Janek, J.R., Bianchini, M., Kondrakov, A., et al. (2022). Single- to few-layer nanoparticle cathode coating for thiophosphate-based all-solid-state batteries. ACS Nano *16*, 18682–18694. https://doi.org/10.1021/acsnano.2c07314.

12. Kong, W.J., Zhao, C.Z., Sun, S., Shen, L., Huang, X.Y., Xu, P., Lu, Y., Huang, W.Z., Huang, J.Q., and Zhang, Q. (2024). From liquid to solid-state batteries: Li-rich Mn-based layered oxides as emerging cathodes with high energy density. Adv. Mater. *36*, e2310738. https://doi.org/10.1002/adma.202310738.

13. Inamoto, J., Enoki, S., Miyamoto, T., Inoo, A., and Matsuo, Y. (2024). Unraveling the Factors of Host Materials Affecting the Kinetics of Electrochemical Anion Intercalation Reaction. ACS Appl. Energy Mater. *7*, 10701–10709. https://doi.org/10.1021/acsaem.4c02440.

14. Zhou, Z., Cazorla, C., Gao, B., Luong, H.D., Momma, T., and Tateyama, Y. (2023). First-principles study on the interplay of strain and state-of-charge with Li-ion diffusion in the battery cathode material $LiCoO_2$. ACS Appl. Mater. Interfaces *15*, 53614–53622. https://doi.org/10.1021/acsami.3c14444.

15. Jousseaume, T., Colin, J.F., Chandesris, M., Lyonnard, S., and Tardif, S. (2024). Strain and collapse during lithiation of layered transition metal oxides: a unified picture. Energy Environ. Sci. *17*, 2753–2764. https://doi.org/10.1039/d3ee04115h.

16. Yu, R., Zeng, W., Zhou, L., Van Tendeloo, G., Mai, L., Yao, Z., and Wu, J. (2023). Layer-by-layer delithiation during lattice collapse as the origin of planar gliding and microcracking in Ni-rich cathodes. Cell Rep. Physiol. Sci. *4*, 101480. https://doi.org/10.2139/ssrn.4332057.

17. Yan, P., Zheng, J., Gu, M., Xiao, J., Zhang, J.-G., and Wang, C.-M. (2017). Intragranular cracking as a critical barrier for high-voltage usage of layer-structured cathode for lithium-ion batteries. Nat. Commun. *8*, 14101. https://doi.org/10.1038/ncomms14101.

18. Ma, Y., Teo, J.H., Kitsche, D., Diemant, T., Strauss, F., Ma, Y., Goonetilleke, D., Janek, J.R., Bianchini, M., and Brezesinski, T. (2021). Cycling performance and limitations of $LiNiO_2$ in solid-state batteries. ACS Energy Lett. *6*, 3020–3028. https://doi.org/10.1021/acsenergylett.1c01447.

19. Ma, Y., Teo, J.H., Walther, F., Ma, Y., Zhang, R., Mazilkin, A., Tang, Y., Goonetilleke, D., Janek, J., Bianchini, M., et al. (2022). Advanced Nanoparticle Coatings for Stabilizing Layered Ni-Rich Oxide Cathodes in Solid-State Batteries. Adv. Funct. Mater. *32*, 2111829. https://doi.org/10.1002/adfm.202111829.

20. Ding, J., Ji, D., Yue, Y., and Smedskjaer, M.M. (2024). Amorphous Materials for Lithium-Ion and Post-Lithium-Ion Batteries. Small *20*, e2304270. https://doi.org/10.1002/smll.202304270.

21. Wei, Z., Wang, D., Yang, X., Wang, C., Chen, G., and Du, F. (2018). From crystalline to amorphous: an effective avenue to engineer high-performance electrode materials for sodium-ion batteries. Adv. Mater. Interfaces *5*, 1800639. https://doi.org/10.1002/admi.201800639.

22. Stachurski, Z.H. (2011). On structure and properties of amorphous materials. Materials (Basel) *4*, 1564–1598. https://doi.org/10.3390/ma4091564.

23. Wu, J., Shen, L., Zhang, Z., Liu, G., Wang, Z., Zhou, D., Wan, H., Xu, X., and Yao, X. (2021). All-solid-state lithium batteries with sulfide electrolytes and oxide cathodes. Electrochem. Energ. Rev. *4*, 101–135. https://doi.org/10.1007/s41918-020-00081-4.

24. Ma, Y., Chen, Y., Jia, J., Cao, P., He, H., and Yao, X. (2025). A NbS_4-Based Nanocomposite Incorporating with $Li_7P_3S_{11}$ and Carbon for Stable All-Solid-State Lithium Batteries. ACS Appl. Energy Mater. *8*, 9781–9787. https://doi.org/10.1021/acsaem.5c01345.

25. Yang, M., Yao, Y., Chang, M., Tian, F., Xie, W., Zhao, X., Yu, Y., and Yao, X. (2023). High Energy Density Sulfur-Rich MoS_6-Based Nanocomposite for Room Temperature All-Solid-State Lithium Metal Batteries. Adv. Energy Mater. *13*, 2300962. https://doi.org/10.1002/aenm.202300962.

26. Sakuda, A., Ohara, K., Fukuda, K., Nakanishi, K., Kawaguchi, T., Arai, H., Uchimoto, Y., Ohta, T., Matsubara, E., Ogumi, Z., et al. (2017). Amorphous metal polysulfides: electrode materials with unique insertion/extraction reactions. J. Am. Chem. Soc. *139*, 8796–8799. https://doi.org/10.1021/jacs.7b03909.

27. Wang, C., Liang, J., Luo, J., Liu, J., Li, X., Zhao, F., Li, R., Huang, H., Zhao, S., Zhang, L., et al. (2021). A universal wet-chemistry synthesis of solid-state halide electrolytes for all-solid-state lithium-metal batteries. Sci. Adv. *7*, eabh1896. https://doi.org/10.1126/sciadv.abh1896.

28. Barajas-Aguilar, A.H., Garay-Tapia, A., Strupiechonski, E., Justo-Guerrero, M.A., Santos-Cruz, J., and Jiménez-Sandoval, S. (2023). Physical insights on the phonon dispersion of TiS_2. Adv. Theory Simul. *6*, 2200821. https://doi.org/10.1002/adts.202200821.

29. Island, J.O., Biele, R., Barawi, M., Clamagirand, J.M., Ares, J.R., Sánchez, C., van der Zant, H.S., Ferrer, I.J., D'Agosta, R., and Castellanos-Gomez, A. (2016). Titanium trisulfide (TiS_3): a 2D semiconductor with quasi-1D optical and electronic properties. Sci. Rep. *6*, 22214. https://doi.org/10.1038/srep22214.

30. Sheriff, K., Cao, Y., Smidt, T., and Freitas, R. (2024). Quantifying chemical short-range order in metallic alloys. Proc. Natl. Acad. Sci. USA *121*, e2322962121. https://doi.org/10.1073/pnas.2322962121.

31. Sharma, S., Singh, S., Singh, R.C., and Sharma, S. (2020). Structural transformation and room temperature ammonia sensing properties of TiS_2 nanostructures. SN Appl. Sci. *2*, 887. https://doi.org/10.1007/s42452-020-2647-x.

32. Sherrell, P.C., Sharda, K., Grotta, C., Ranalli, J., Sokolikova, M.S., Pesci, F.M., Palczynski, P., Bemmer, V.L., and Mattevi, C. (2018). Thickness-dependent characterization of chemically exfoliated TiS_2 nanosheets. ACS Omega *3*, 8655–8662. https://doi.org/10.1021/acsomega.8b00766.

33. Lin, Z., Mao, M., Yang, C., Tong, Y., Li, Q., Yue, J., Yang, G., Zhang, Q., Hong, L., Yu, X., et al. (2021). Amorphous anion-rich titanium polysulfides for aluminum-ion batteries. Sci. Adv. *7*, eabg6314. https://doi.org/10.1126/sciadv.abg6314.

34. Matsuyama, T., Deguchi, M., Mitsuhara, K., Ohta, T., Mori, T., Orikasa, Y., Uchimoto, Y., Kowada, Y., Hayashi, A., and Tatsumisago, M. (2016). Structure analyses using X-ray photoelectron spectroscopy and X-ray absorption near edge structure for amorphous MS_3 (M: Ti, Mo) electrodes in all-solid-state lithium batteries. J. Power Sources *313*, 104–111. https://doi.org/10.1016/j.jpowsour.2016.02.044.

35. Ozaki, F., Tanaka, S., Choi, Y., Osada, W., Mukai, K., Kawamura, M., Fukuda, M., Horio, M., Koitaya, T., Yamamoto, S., et al. (2023). Hydrogen-induced sulfur vacancies on the MoS_2 basal plane studied by ambient pressure XPS and DFT calculations. ChemPhysChem *24*, e202300477. https://doi.org/10.1002/cphc.202300477.

36. Dolui, K., and Sanvito, S. (2016). Dimensionality-driven phonon softening and incipient charge density wave instability in TiS_2. Europhys. Lett. *115*, 47001. https://doi.org/10.1209/0295-5075/115/47001.

37. Liu, S., Xiao, W., Zhong, M., Pan, L., Wang, X., Deng, H.-X., Liu, J., Li, J., and Wei, Z. (2018). Highly polarization sensitive photodetectors based on quasi-1D titanium trisulfide (TiS_3). Nanotechnology *29*, 184002. https://doi.org/10.1088/1361-6528/aaafa2.

38. Chang, B.-Y., and Park, S.-M. (2010). Electrochemical impedance spectroscopy. Annu. Rev. Anal. Chem. (Palo Alto. Calif) *3*, 207–229. https://doi.org/10.1146/annurev.anchem.012809.102211.

39. Cui, L., Zhang, S., Ju, J., Liu, T., Zheng, Y., Xu, J., Wang, Y., Li, J., Zhao, J., Ma, J., et al. (2024). A cathode homogenization strategy for enabling long-cycle-life all-solid-state lithium batteries. Nat. Energy *9*, 1084–1094. https://doi.org/10.1038/s41560-024-01596-6.

40. Van Nghia, N., Bien, T.T., Long, N.T., and Dang, M.T. (2025). First-principles insights into sulfur and nitrogen co-doped Ti_2CO_2 MXene as an advanced anchoring material for sodium polysulfides in sodium–sulfur batteries. RSC Adv. *15*, 35586–35597. https://doi.org/10.1039/d5ra05003k.

41. Lu, Y., Zhao, C.-Z., Huang, J.-Q., and Zhang, Q. (2022). The timescale identification decoupling complicated kinetic processes in lithium batteries. Joule *6*, 1172–1198. https://doi.org/10.1016/j.joule.2022.05.005.

42. Hori, S., Kanno, R., Sun, X., Song, S., Hirayama, M., Hauck, B., Dippon, M., Dierickx, S., and Ivers-Tiffée, E. (2023). Understanding the impedance spectra of all-solid-state lithium battery cells with sulfide superionic conductors. J. Power Sources *556*, 232450. https://doi.org/10.1016/j.jpowsour.2022.232450.

43. Malik, Y.T., Braig, M., Simon, P., Zeis, R., and Fleischmann, S. (2024). Analysis of battery-like and pseudocapacitive ion intercalation kinetics via distribution of relaxation times. J. Electrochem. Soc. *171*, 110515. https://doi.org/10.1149/1945-7111/ad8d51.

44. Fleischmann, S., Shao, H., Taberna, P.-L., Rozier, P., and Simon, P. (2021). Electrochemically induced deformation determines the rate of lithium intercalation in bulk TiS_2. ACS Energy Lett. *6*, 4173–4178. https://doi.org/10.1021/acsenergylett.1c01934.

45. Verma, A., Smith, K., Santhanagopalan, S., Abraham, D., Yao, K.P., and Mukherjee, P.P. (2017). Galvanostatic intermittent titration and performance based analysis of $LiNi_{0.5}Co_{0.2}Mn_{0.3}O_2$ cathode. J. Electrochem. Soc. *164*, A3380–A3392. https://doi.org/10.1149/2.1701713jes.

46. Hong, C., Leng, Q., Zhu, J., Zheng, S., He, H., Li, Y., Liu, R., Wan, J., and Yang, Y. (2020). Revealing the correlation between structural evolution and Li^+ diffusion kinetics of nickel-rich cathode materials in Li-ion batteries. J. Mater. Chem. A *8*, 8540–8547. https://doi.org/10.1039/d0ta00555j.

47. Moutaabbid, H., Taverna, D., Pelloquin, D., Paulatto, L., Gloter, A., Guéron, S., Kasumov, A., and Gauzzi, A. (2026). A Metallic CrS_2 Phase Bridging the Gap between Two-And Three-Dimensional Dichalcogenides. Preprint at arXiv. https://doi.org/10.48550/arXiv.2604.08695.

48. Zhang, L., Sun, D., Kang, J., Wang, H.-T., Hsieh, S.-H., Pong, W.-F., Bechtel, H.A., Feng, J., Wang, L.-W., Cairns, E.J., et al. (2018). Tracking the chemical and structural evolution of the TiS_2 electrode in the lithium-ion cell using operando X-ray absorption spectroscopy. Nano Lett. *18*, 4506–4515. https://doi.org/10.1021/acs.nanolett.8b01680.

49. Gao, J., Hua, M., Lu, J., Qin, Y., Zhang, S., Li, Q., Yang, L., Wang, C., Lin, X., Sun, Y., et al. (2026). Cation-Disordered Rock-Salt Lithium Titanium Oxyfluoride Anode Enabling High-Rate Li-Ion Storage Through a 3D Percolation Network. Nano-Micro Lett. *18*, 277. https://doi.org/10.1007/s40820-026-02123-w.

50. Peng, W.-C., Chen, Y.-C., He, J.-L., Ou, S.-L., Horng, R.-H., and Wuu, D.-S. (2018). Tunability of p-and n-channel TiO_x thin film transistors. Sci. Rep. *8*, 9255. https://doi.org/10.1038/s41598-018-27598-5.

51. Serbessa, G.G., Taklu, B.W., Nikodimos, Y., Temesgen, N.T., Muche, Z.B., Merso, S.K., Yeh, T.-I., Liu, Y.-J., Liao, W.-S., Wang, C.-H., et al. (2024). Boosting the interfacial stability of the Li_6PS_5Cl electrolyte with a Li anode via in situ formation of a LiF-rich SEI layer and a ductile sulfide composite solid electrolyte. ACS Appl. Mater. Interfaces *16*, 10832–10844. https://doi.org/10.1021/acsami.3c14763.

52. Li, T., Huang, S., Kane, N., Wang, J.-H., Luo, Z., Zhang, W., Nam, G., Zhao, B., Qi, Y., and Liu, M. (2023). Operando Raman and DFT analysis of (de) lithiation in fast-charging, shear-phase H-Nb_2O_5. ACS Energy Lett. *8*, 3131–3140. https://doi.org/10.1021/acsenergylett.3c01031.

53. Ma, Y., Zhang, R., Ma, Y., Diemant, T., Tang, Y., Payandeh, S., Goonetilleke, D., Kitsche, D., Liu, X., Lin, J., et al. (2024). Interface and electrode microstructure engineering for optimizing performance of the $LiNiO_2$ cathode in all-solid-state batteries. Chem. Mater. *36*, 2588–2598. https://doi.org/10.1021/acs.chemmater.4c00301.

54. Zuo, T.T., Walther, F., Teo, J.H., Rueß, R., Wang, Y., Rohnke, M., Schröder, D., Nazar, L.F., and Janek, J. (2023). Impact of the Chlorination of Lithium Argyrodites on the Electrolyte/Cathode Interface in Solid-State Batteries. Angew. Chem. Int. Ed. *62*, e202213228. https://doi.org/10.1002/anie.202213228.

55. Hood, Z.D., Mane, A.U., Sundar, A., Tepavcevic, S., Zapol, P., Eze, U.D., Adhikari, S.P., Lee, E., Sterbinsky, G.E., Elam, J.W., et al. (2023). Multifunctional Coatings on Sulfide-Based Solid Electrolyte Powders with Enhanced Processability, Stability, and Performance for Solid-State Batteries. Adv. Mater. *35*, e2300673. https://doi.org/10.1002/adma.202300673.

56. Shinoda, M., Matsunoshita, K., Nakayama, M., Hiroi, S., Ohara, K., Abe, M., Ishiguro, N., Takahashi, Y., Hasegawa, G., Kuwata, N., et al. (2025). Activation of Anionic Redox for Stoichiometric and Li-Excess Metal Sulfides through Structural Disordering: Joint Experimental and Theoretical Study. J. Am. Chem. Soc. *147*, 26238–26253. https://doi.org/10.1021/jacs.5c04018.

57. Kresse, G., and Hafner, J. (1993). Ab initio molecular dynamics for liquid metals. Phys. Rev., B *47*, 558–561. https://doi.org/10.1016/0022-3093(95)00355-X.

58. Kresse, G., and Furthmüller, J. (1996). Efficient iterative schemes for ab initio total-energy calculations using a plane-wave basis set. Phys. Rev. B Condens. Matter *54*, 11169–11186. https://doi.org/10.1103/PhysRevB.54.11169.

59. Kresse, G., and Joubert, D. (1999). From ultrasoft pseudopotentials to the projector augmented-wave method. Phys. Rev., B *59*, 1758–1775. https://doi.org/10.1103/PhysRevB.59.1758.

60. Blöchl, P.E. (1994). Projector augmented-wave method. Phys. Rev. B Condens. Matter *50*, 17953–17979. https://doi.org/10.1103/PhysRevB.50.17953.

61. Perdew, J.P., Burke, K., and Ernzerhof, M. (1996). Generalized gradient approximation made simple. Phys. Rev. Lett. *77*, 3865–3868. https://doi.org/10.1103/PhysRevLett.77.3865.

62. Grimme, S., Antony, J., Ehrlich, S., and Krieg, H. (2010). A consistent and accurate ab initio parametrization of density functional dispersion correction (DFT-D) for the 94 elements H-Pu. J. Chem. Phys. *132*, 154104. https://doi.org/10.1063/1.3382344.

63. Nosé, S. (1984). A unified formulation of the constant temperature molecular dynamics methods. J. Chem. Phys. *81*, 511–519. https://doi.org/10.1063/1.447334.

64. Hoover, W.G. (1985). Canonical dynamics: Equilibrium phase-space distributions. Phys. Rev. A Gen. Phys. *31*, 1695–1697. https://doi.org/10.1103/PhysRevA.31.1695.

65. Ong, S.P., Richards, W.D., Jain, A., Hautier, G., Kocher, M., Cholia, S., Gunter, D., Chevrier, V.L., Persson, K.A., and Ceder, G. (2013). Python Materials Genomics (pymatgen): A robust, open-source python library for materials analysis. Comput. Mater. Sci. *68*, 314–319. https://doi.org/10.1016/j.commatsci.2012.10.028.

66. Zhu, Y., He, X., and Mo, Y. (2016). First principles study on electrochemical and chemical stability of solid electrolyte–electrode interfaces in all-solid-state Li-ion batteries. J. Mater. Chem. A *4*, 3253–3266. https://doi.org/10.1039/C5TA08574H.